The elasto-plastic response of underground excavations in rock masses that satisfy the Hoek–Brown failure criterion

C. Carranza-Torres [a,*], C. Fairhurst [b]

[a]*Itasca Consulting Group, Suite 310, 708 South Third Street, Minneapolis, MN 55415, USA*
[b]*University of Minnesota, Minneapolis, MN, USA*

Abstract

This paper is intended to illustrate the relationship between the Hoek–Brown parameters describing the strength of rock masses and the mechanical response of underground openings.

A formulation of the elasto-plastic behavior of rock in terms of the Hoek–Brown criterion is presented. The analysis assumes that the joint system present in the rock mass has no preferred orientation so that the medium can be considered to behave as an isotropic continuum. It is shown that appropriate scaling of the Hoek–Brown parameters leads to considerable simplification in defining the elasto-plastic response of the rock mass.

The classical case in which the excavation process is treated as a uniform reduction of internal pressure in symmetrically loaded cylindrical and spherical cavities is considered. Closed-form expressions are given for the extent of plastic behavior and the related stress and displacement fields. A dimensionless graphical representation of these solutions is provided that allows accurate estimates of the response of excavations in Hoek–Brown materials to be made quickly and easily. Examples are given to illustrate the use of the graphs.

Illustrative applications of the derived closed-form solutions are also described. The construction of ground reaction curves for the design of cylindrical tunnels according to the convergence–confinement method and a case study of stability analysis of spherical cavities produced by underground nuclear explosions in French Polynesian atolls are discussed. © 1999 Elsevier Science Ltd. All rights reserved.

1. Introduction

The Hoek–Brown criterion attempts to address one of the main problems in the practical design of large structures in or on rock masses. The presence of joints and associated in situ geological effects (e.g. weathering and inhomogeneities) can considerably reduce the mechanical properties of the rock mass compared to those of intact specimens taken from the mass. Because it is not possible to make tests directly on the large-scale mass, some type of *estimate* of the large-scale mechanical properties is needed in order to proceed with a rational analysis for design.

The Hoek–Brown criterion has found wide practical application as a method of defining the stress conditions under which a rock mass will deform inelastically and, if not supported adequately, collapse. The criterion applies for isotropic behavior. It does not apply to materials that exhibit significant anisotropy in strength and deformability (e.g. if the rock mass contains a single dominant joint direction). In such cases a treatment with anisotropic continuum models or discontinuum models is more appropriate.

For cases in which the assumptions of isotropic behavior are reasonable, the parameters defining the Hoek–Brown criterion can be estimated from a combination of laboratory tests on intact rock cores and an 'adjustment' to account for the reduced strength of the rock mass due to the presence of weaknesses and jointing. This adjustment is usually performed using empiri-

* Corresponding author. Tel.: +1-612-371-4711; fax: +1-612-371-4717.

E-mail address: icg@itascacg.com (C. Carranza-Torres)

a)

ROCK TYPE	σ_{ci} [MPa]	ν	E [GPa]	G [GPa]
Basalt (Nevada Test Site)	148	0.32	35	13
Gneiss (Orofino, Idaho)	162	0.34	54	20
Granite (Nevada Test Site)	141	0.22	74	30
Limestone (Bedford, Indiana)	51	0.29	29	11
Quartzite (Baraboo, Wisconsin)	320	0.11	88	40
Sandstone (Berea, Amherst, Ohio)	74	0.38	19	7
Siltstone (Hackensack, New Jersey)	123	0.22	26	11
Tuff (Nevada Test Site)	11	0.29	4	1

b)

Rock type	Class	Group	Texture		
			Coarse	Medium	Fine
SEDIMENTARY	Clastic		Conglomerate (22)	Sandstone (19)	Siltstone (9)
SEDIMENTARY	Non-clastic	Organic		Coal (8~21)	
SEDIMENTARY	Non-clastic	Carbonate	Breccia (20)	Limestone (8~10)	
METAMORPHIC	Non-foliated		Marble (9)	Hornfels (19)	Quartzite (24)
METAMORPHIC	Slightly foliated		Migmatite (30)	Amphibolite (25~31)	Mylonites (6)
METAMORPHIC	Foliated		Gneiss (33)	Schists (4~8)	Phyllites (10)
IGNEOUS	Light		Granite (33)		Rhyolite (16)
IGNEOUS	Light		Granodiorite (30)		Dacite (17)
IGNEOUS	Dark		Gabbro (27)	Dolerite (19)	Basalt (17)
IGNEOUS	Extrusive pyroclastic		Agglomerate (20)	Breccia (18)	Tuff (15)

Fig. 1. (a) Reference values for unconfined compressive strength (σ_{ci}), Poisson's ratio (ν), Young's modulus (E) and Shear modulus (G) for different rock types (adapted from Goodman [14]); (b) Reference values for the coefficient m_i for different rock types (adapted from Hoek and Brown [17]). The values of m_i is shown in parentheses below the name of the rock.

cal rules that account for the quality of the rock mass. A detailed discussion of the process of characterization can be found in Hoek and Brown [17]. Examples of case histories supporting the validity of the approach are reported by Moretto et al. [28] and Karzulovic and Diaz [25], among others.

Although the complex geometries of many geotechnical design problems dictate the use of numerical modeling to provide 'more realistic' results than those from classical analytical solutions, the insight into the general nature of the solution (influence of the variables involved, etc.) that can be gained from the classi-
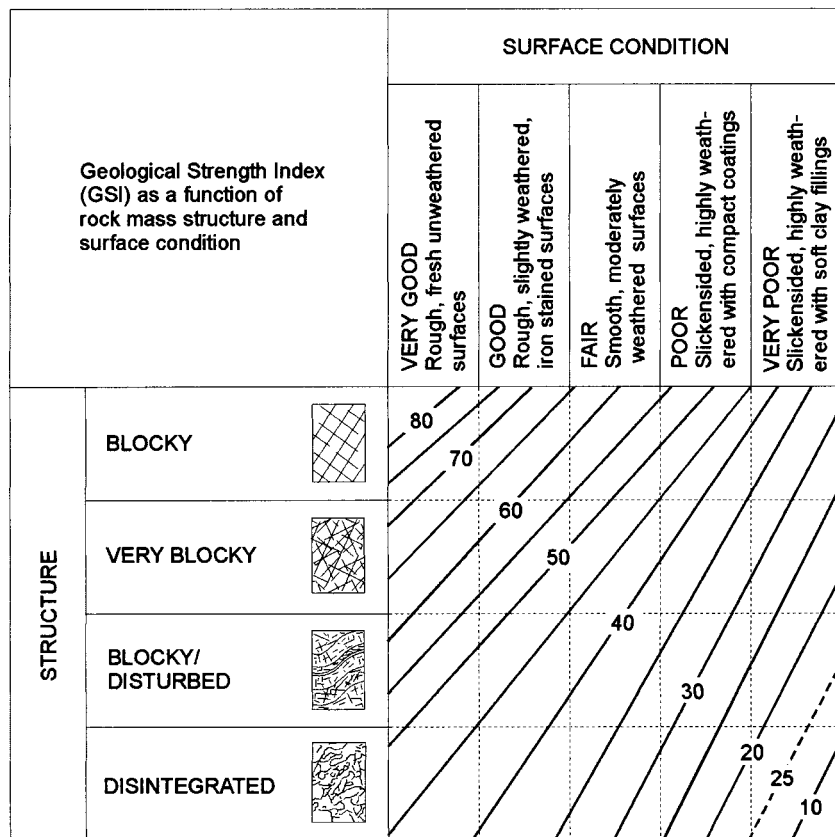
Fig. 2. Empirical chart for the estimation of the geological strength index (GSI) based on the characteristics of the rock mass (adapted from Hoek and Brown [17]).

cal solution is an important attribute that should not be overlooked. Some degree of simplification is always needed in formulating a design analysis and it is essential that the design engineer be able to assess the general 'correctness' of a numerical analysis wherever possible. The closed-form results provide a valuable means of making this assessment.

The closed-form solutions that describe the elasto-plastic behavior around circular and spherical cavities are among the most widely used for general design assessment, especially with respect to tunnel excavations and support design. This paper describes a dimensionless formulation of the Hoek–Brown criterion that allows the criterion to be coupled directly to the classical solutions, with the result that estimates of practical concerns such as extent of the inelastic zone, effect of support pressure, etc. can be made immediately, once the appropriate Hoek–Brown parameters for the rock mass have been defined.

2. The Hoek–Brown failure criterion

Testing of rock specimens under triaxial loading allows the combination of stresses that lead to inelastic deformation and, ultimately, collapse of the specimen to be determined. The ultimate strength of rock subjected to triaxial loading is known to depend on the applied confining pressure. The relationship between the strength and confining pressure is also known to be nonlinear.

The Hoek–Brown failure criterion for intact rock samples approximates the nonlinear relationship between the maximum axial stress, σ_1, that can be sustained by the sample and the applied confining stress, σ_3. The relationship is defined by the following parabolic law (see for example Hoek and Brown [16]),

$$\sigma_1 = \sigma_3 + \sigma_{ci}\sqrt{m_i\frac{\sigma_3}{\sigma_{ci}} + 1} \tag{1}$$

where σ_{ci} is the unconfined compressive strength of the rock sample and m_i is a parameter deduced from the σ_1 versus σ_3 test results for a particular rock type.

In order to characterize the intact rock according to the Hoek–Brown criterion, it is necessary to define the parameters σ_{ci} and m_i. Hoek et al. [19] have suggested methods for fitting the parabola defined by Eq. (1) to the scattered (σ_1, σ_3) data obtained from triaxial tests. Alternatively, when triaxial testing is not possible, the parameters can be estimated from empirical charts.
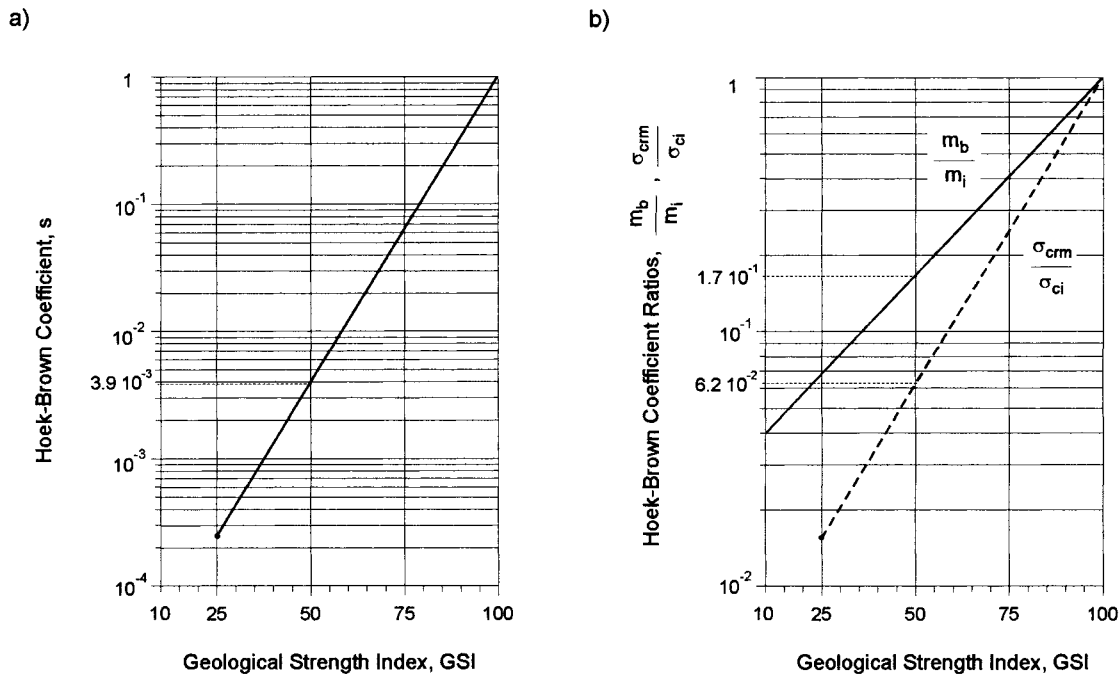
a)

b)

Fig. 3. (a) Hoek–Brown coefficient *s* as a function of the geological strength index (GSI); (b) Ratios m_b/m_i and σ_{cm}/σ_{ci} as a function of GSI. For any value of GSI < 25, the parameter *s* and the ratio σ_{cm}/σ_{ci} are both identically zero.

For reference purposes, Figs. 1a,b (adapted from Goodman [14] and Hoek and Brown [17], respectively) show typical values of σ_{ci} and m_i for different rock types.

As noted earlier, joints and defects in a rock mass reduce the strength of the mass below the strength of an intact specimen of the same rock type (Hoek et al. [18]). By using the so-called geological strength index (GSI) as a 'scaling' parameter, the Hoek–Brown criterion for the strength of intact cores in triaxial tests, as shown in Eq. (1), can be adjusted to provide an estimate of the decreased strength of the rock mass in situ. The GSI is an empirically derived dimensionless number that varies over a range between 10 and 100 (Hoek et al. [19]) and which can be estimated by examination of the quality of the rock mass in situ by direct inspection of an outcrop, for example.

Figure 2 (adapted from Hoek and Brown [17]) shows how the GSI can be estimated from the structure and surface conditions of the rock mass. By definition, GSI values close to 10 correspond to very poor quality rock mass, while GSI values close to 100 correspond to excellent quality rock masses (for which the rock mass strength is equal to the intact rock strength).

The value GSI = 25 is significant in the sense that it indicates the limit between rock masses of very poor quality (GSI < 25) and those of good to reasonable quality (GSI > 25). According to Hoek and Brown [17], the choice of the value GSI = 25 to distinguish between these rock qualities is arbitrary; the limit at

which the rock mass falls into the category of 'very poor' could have been taken to be some other number close to this value. As will be seen later, there is a clear difference in the mechanical behavior of rock masses with GSI values below and above this limit. For rock masses of good to reasonable quality (i.e. GSI > 25) the Geological Strength Index is equivalent to the rock mass rating (RMR) introduced by Bieniawski [3] when the rating for *Groundwater* is assessed as 'dry' and the rating for *Joint Orientation* as 'favorable'.

When the GSI scale factor is introduced, the Hoek–Brown failure criterion for the rock mass is given by (Hoek and Brown [17])

$$\sigma_1 = \sigma_3 + \sigma_{ci}\left(m_b\frac{\sigma_3}{\sigma_{ci}} + s\right)^a \tag{2}$$

The parameter m_b in Eq. (2) depends on both the intact rock parameter m_i (of Eq. (1)) and the value of GSI introduced above, as defined by the equation

$$m_b = m_i\exp\left(\frac{\text{GSI} - 100}{28}\right) \tag{3}$$

The parameters *s* and *a*, also depend empirically on the value of GSI as follows, for GSI ≥ 25,

$$s = \exp\left(\frac{\text{GSI} - 100}{9}\right); \quad a = 0.5 \tag{4}$$
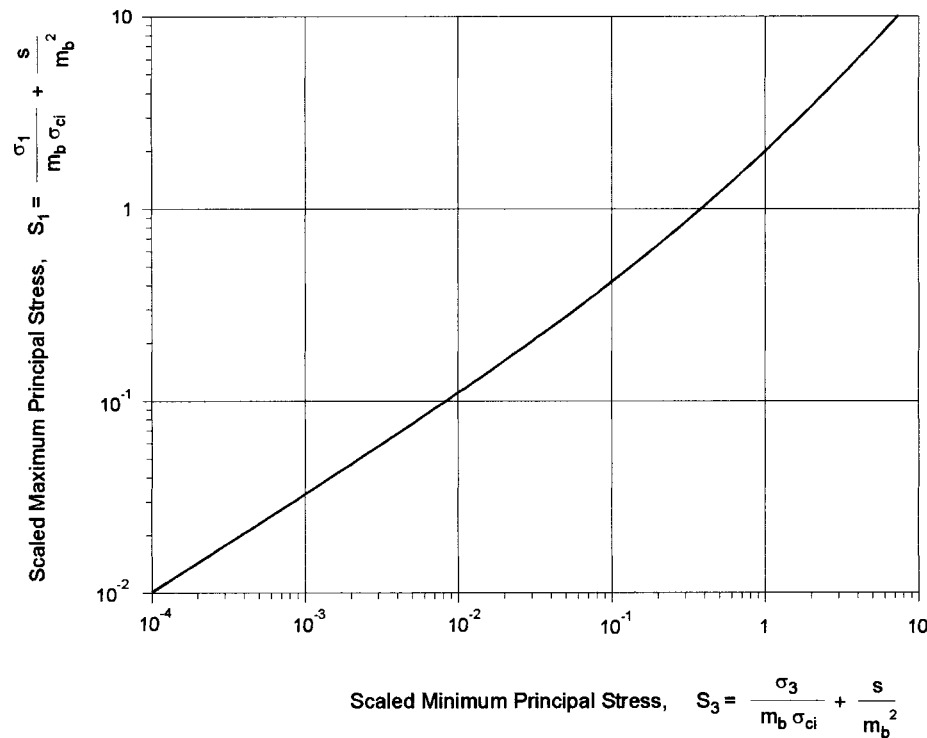
and for *GSI* < 25,

Fig. 4. Scaled (dimensionless) form of the Hoek–Brown failure criterion in terms of the scaled maximum and minimum principal stresses S_1 and S_3 respectively. The rock-mass failure criterion is characterized by three parameters: the unconfined compressive strength of the intact rock specimen, σ_{ci} and the coefficients s and m_b (the parameters s and m_b can be determined from Fig. 3 when the GSI value is known). The exponent a is assumed to be 0.5.

$$s = 0; \quad a = 0.65 - \frac{\text{GSI}}{200} \qquad (5)$$

The diagrams in Fig. 3 show, in graphical form, Eqs. (3)–(5) as a function of the GSI. When GSI = 100 (the hypothetical case in which the rock mass has the same strength as the intact rock sample), the parameters are $s = 1$, $m_b = m_i$ and $a = 0.5$. With these values, the yield condition for the rock mass (Eq. (2)) and for the intact rock (Eq. (1)) are the same.

As mentioned earlier, the unconfined compressive strength of the intact rock, σ_{ci}, corresponds to the strength of a rock sample under zero confining pressure — i.e. the strength obtained by setting $\sigma_3 = 0$ in Eq. (1). Similarly, the unconfined compressive strength for the rock mass, σ_{crm}, can be defined by setting $\sigma_3 = 0$ in Eq. (2); the expression for the strength then becomes

$$\sigma_{crm} = \sigma_{ci} s^a \qquad (6)$$

Thus, for the general case in which the GSI < 100, the unconfined compressive strength of the rock mass as given by Eq. (6) is smaller than the unconfined compressive strength of the intact rock by the factor s^a. The ratio σ_{crm}/σ_{ci}, plotted in Fig. 3b, shows that the rock mass has zero unconfined compressive strength whenever GSI falls below the critical limit 25. The im-

portance of this observation will be discussed in the next section.

The Hoek–Brown criterion defined by Eq. (2) can be conveniently re-scaled to obtain a unique relationship that is independent of the parameters σ_{ci}, m_b and s (Londe [26]). The use of transformations of this type is common in plastic analysis. For example, Anagnostou and Kovari [1] show how particular re-scaling of the field quantities in elasto-plastic problems involving Mohr–Coulomb materials allows the cohesion to be 'hidden', resulting in a simpler formulation of the governing equations.

The transformation suggested by Londe [26] applies to the particular case $a = 0.5$ and involves dividing the stress magnitudes by $m_b\sigma_{ci}$ and adding the term s/m_b^2. This particular form of scaling is justified by observing the form of Eq. (2) when both sides are divided by $m_b\sigma_{ci}$; i.e.

$$\frac{\sigma_1}{m_b\sigma_{ci}} = \frac{\sigma_3}{m_b\sigma_{ci}} + \left(\frac{\sigma_3}{m_b\sigma_{ci}} + \frac{s}{m_b^2}\right)^{0.5} \qquad (7)$$

Thus, from Eq. (7), the scaled principal stresses S_1 and S_3 are defined naturally as,

$$S_1 = \frac{\sigma_1}{m_b\sigma_{ci}} + \frac{s}{m_b^2} \qquad S_3 = \frac{\sigma_3}{m_b\sigma_{ci}} + \frac{s}{m_b^2} \qquad (8)$$
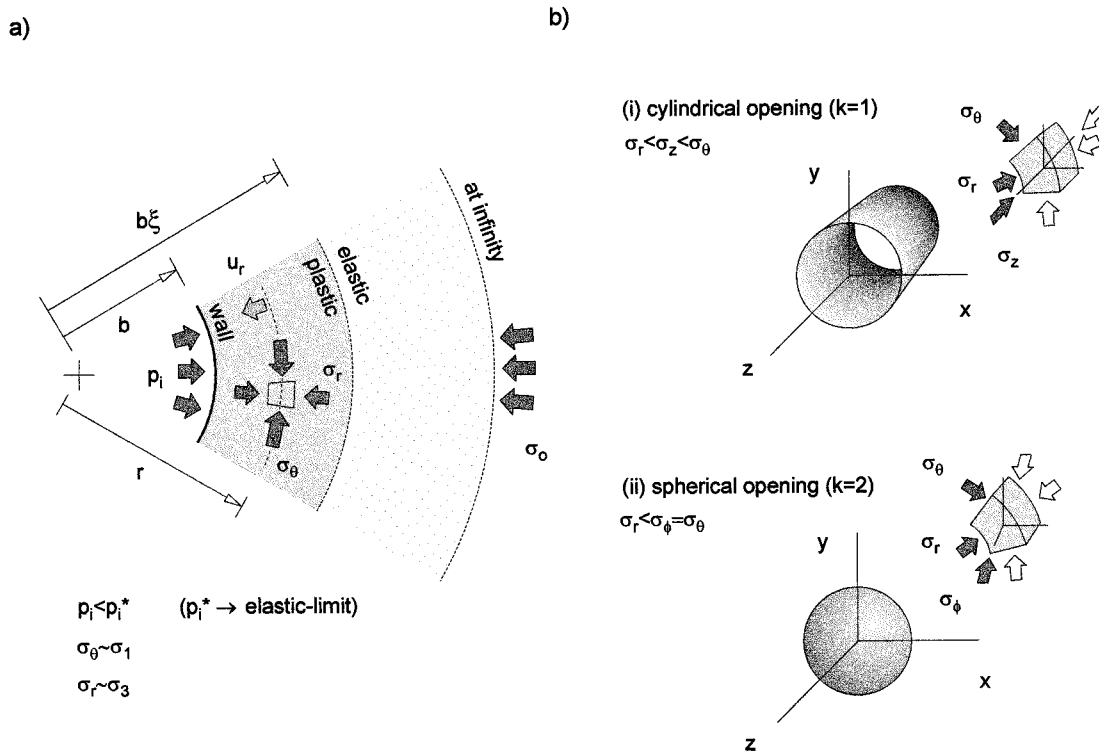
a)

b)

Fig. 5. (a) Stress and displacement fields in the plastic region around a circular (two or three dimensional) opening; (b) Principal stresses for (i) cylindrical and (ii) spherical openings.

When expressed in terms of S_1 and S_3, the failure criterion for the rock mass (Eq. (2)) takes the simple form,

$$S_1 = S_3 + \sqrt{S_3} \qquad (9)$$

It should be emphasized that Eq. (9) is strictly valid only when the parameter a in Eq. (2) is equal to 0.5. According to Eq. (4), $a = 0.5$ for the broad range of situations in which GSI $\geq$ 25 (Fig. 2).

Londe's 're-scaled' Hoek–Brown failure criterion, given by Eq. (9), is of general applicability. Since the parameters σ_{ci}, m_b and s are 'hidden' in the relationship, Eq. (9) applies to any type of rock that is assumed to obey the Hoek–Brown criterion. This can be seen in Fig. 4, where the Hoek–Brown parabola is represented by a single curve in the reference system of scaled principal stresses.

The use of Eq. (9) rather than Eq. (2) can lead to important simplifications in the analysis of stresses and deformations in rock masses. This will be illustrated in Section 4 of this paper, when considering the problem of cylindrical and spherical cavities excavated in 'Hoek–Brown' materials.

3. Elasto-plastic solution for excavation of cylindrical and spherical openings in 'Hoek–Brown' materials

This problem is of particular importance in rock engineering. When applied to cylindrical cavities, it is the basis for the practical design of supports in tunnels using the so-called 'Convergence–Confinement' method (Section 4.1). The solution for spherical cavities is useful in assessing the stability of the unsupported region in the vicinity of the tunnel face (for example, Mühlhaus [29]) or in assessing the stability of cavities created by underground explosions (Section 4.2).

The problem of stresses and deformations around underground cylindrical excavations has been considered by numerous authors in the past. Brown et al. [5] presented a thorough review of elasto-plastic solutions available at the time of their paper and derived a number of closed-form solutions for 'Hoek–Brown' materials. These solutions included some simplifying assumptions (specifically in the formulation for displacements). Later authors have reported differences when comparing some of the results by Brown et al. with those obtained using more rigorous elasto-plastic numerical analyses. For example, Wang [35] identified sources of discrepancy in the solution by Brown et al.
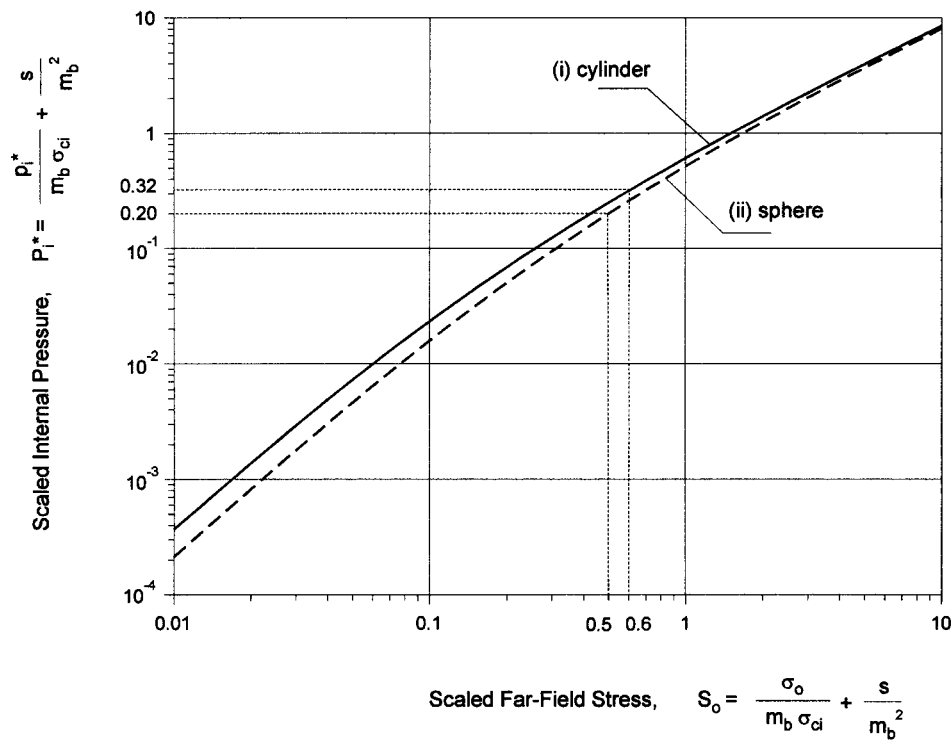
Fig. 6. Scaled critical (internal) pressure P_i^*, for which the elastic limit of the rock mass is reached as a function of the scaled far-field stress, S_o. ('Scaled' in this and later figures implies dimensionless scaling). The two shown curves correspond to (i) cylindrical and (ii) spherical excavations in a Hoek–Brown material (σ_o is the actual far-field stress; the parameters σ_{ci}, s and m_b define the failure criterion of the rock mass).

and presented a numerical solution for the correct constitutive equations.

Hoek et al. [19] and Hoek [20] have recently proposed an alternative method of calculation in which equivalent frictional parameters are derived statistically and then used in elasto-plastic solutions for a linear Mohr–Coulomb criterion.

Several recent authors have considered ways in which to generalize elasto-plastic problems involving symmetrical geometries. Collins and Stimpson [8] present a general (mechanical) self-similar solution based on the deformation theory of plasticity that applies to the case of expansion of cavities. Papanastasiou and Durban [32] present an elasto-plastic analysis based on the deformation theory of plasticity for Drucker–Prager materials.

In the present study, the problem will be approached using a solution derived in Carranza-Torres [6]. This solution uses the incremental theory of plasticity in combination with properties of mechanical self-similarity. The approach is of general applicability in the sense that it can account for any type of yield condition or flow rule. In this particular case, the formulation is adapted to account for materials that begin to yield as determined by the Hoek–Brown criterion and that may or may not exhibit associated flow in the plastic regime.

The problem to be examined is represented in Fig. 5a.

The goal is to solve for the stresses and displacements in the plastic and elastic regions around cylindrical or spherical openings of radius b. (In elasto-plastic solutions involving circular cavities, the variable 'a' is often used to designate the radius of the cavity and 'b' to designate the radius of the elasto-plastic interface; here, the radius of the cavity is designated by b to avoid confusion with the parameter a in the Hoek–Brown criterion).

The cavities are assumed to be subject, initially (i.e. before they are created), to an internal pressure, p_i and a far-field stress, σ_o. The effect of a monotonic reduction of the internal pressure p_i, from the initial value σ_o, is considered. The limit between the elastic and plastic regions (i.e. the radius $b\xi$) is also to be determined. As shown in Fig. 5b, the symmetry of the problem allows a single formulation that can be applied to either cylindrical or spherical cavities. In the analysis that follows, the parameter $k = 1$ defines a cylindrical cavity and the parameter $k = 2$ defines a spherical cavity. (In formulating the problem for cylindrical openings, the out-of-plane stress has been assumed to be the intermediate principal stress).

In order not to obscure the discussion of the practical application of the method, mathematical details of the analyses are presented separately in the Appendix to this paper. The main results are considered below
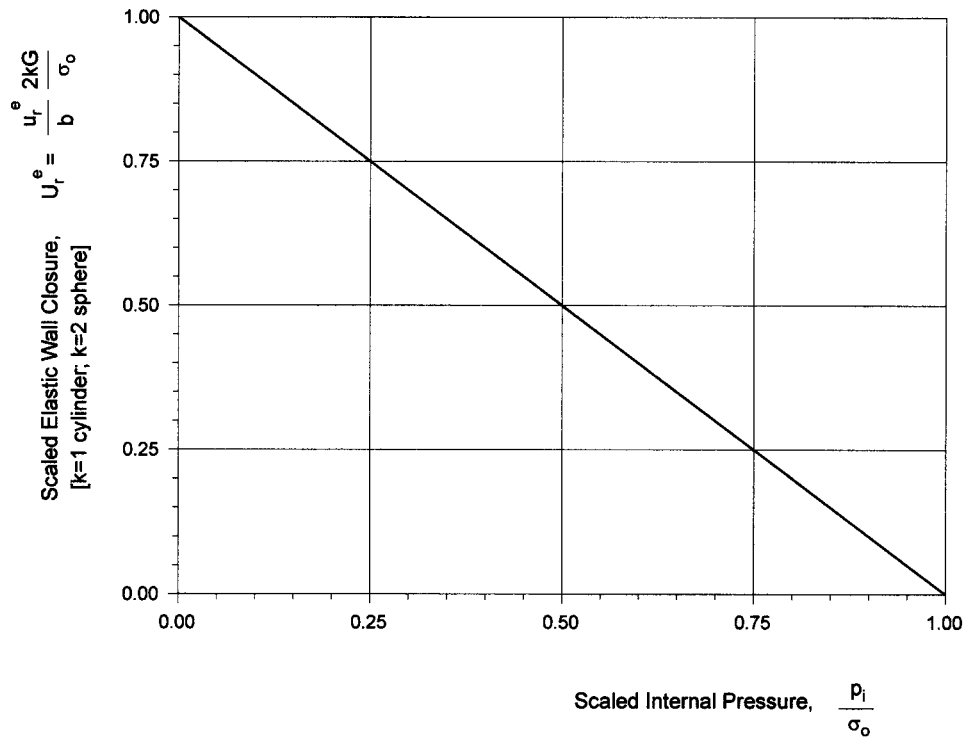
Fig. 7. Scaled wall radial displacement, U_r^e, as a function of scaled internal pressure, p_i/σ_o, for cylindrical or spherical openings in elastic materials. (b is the radius of the cavity, σ_o and p_i are the uniform far-field stress and internal pressure, respectively and G is the shear modulus of the material). Note: 'b' is used for the radius of the cavity — rather than the more customary 'a' since a is used as an exponent in the Hoek–Brown criterion (Eq. (2)).

and application examples are presented later in Section 4.

To make the solution of general applicability, the scaling transformation discussed in the last section will be applied to the internal pressure, p_i and the far-field stresses, σ_o. This results in the scaled (dimensionless) internal pressure, P_i and the scaled (dimensionless) far-field stress, S_o:

$$P_i = \frac{p_i}{m_b\sigma_{ci}} + \frac{s}{m_b^2} \quad S_o = \frac{\sigma_o}{m_b\sigma_{ci}} + \frac{s}{m_b^2} \tag{10}$$

An expression for the critical scaled internal pressure, P_i^*, at which plastic deformation first starts to develop around the opening is given by [see Eq. (A.57) in the Appendix],

$$P_i^* = \left[\frac{k - \sqrt{k^2 + 4(k+1)^2 S_o}}{2(k+1)} \right]^2 \tag{11}$$

The relationship in Eq. (11) is shown graphically in Fig. 6 for values of S_o ranging from 0.01 to 10. These limits should cover the range of values likely to be encountered in practice.

When the scaled internal pressure, P_i, is larger than the critical value, P_i^*, (i.e. $P_i^* < P_i < S_o$), the medium around the cavity remains elastic. In this case, the induced radial displacement at the wall (i.e. the value

of u_r at $r = b$) is defined by Lamé's solution (as given by Eq. (A.3)), as

$$u_r^e = \frac{\sigma_o - p_i}{2kG} b \tag{12}$$

As seen from Eq. (12), the resulting elastic displacement (u_r^e) depends on the shear modulus (G) of the material and on the external and internal boundary stresses (i.e. σ_o and p_i respectively). Eq. (12) can be rewritten as

$$U_r^e = 1 - \frac{p_i}{\sigma_o} \tag{13}$$

where U_r^e is defined as

$$U_r^e = \frac{u_r^e}{b} \frac{2kG}{\sigma_o} \tag{14}$$

The relationship (Eq. (13)) is plotted in Fig. 7.

When the scaled internal pressure (P_i) is below the critical value P_i^* (i.e. $P_i < P_i^*$), a plastic region of radial extent $b\xi$ develops around the opening. The dimensionless parameter ξ (which expresses the size of the failed region as a proportion of the radius of the cavity) is defined in Eq. (A.60), repeated here as Eq. (15)

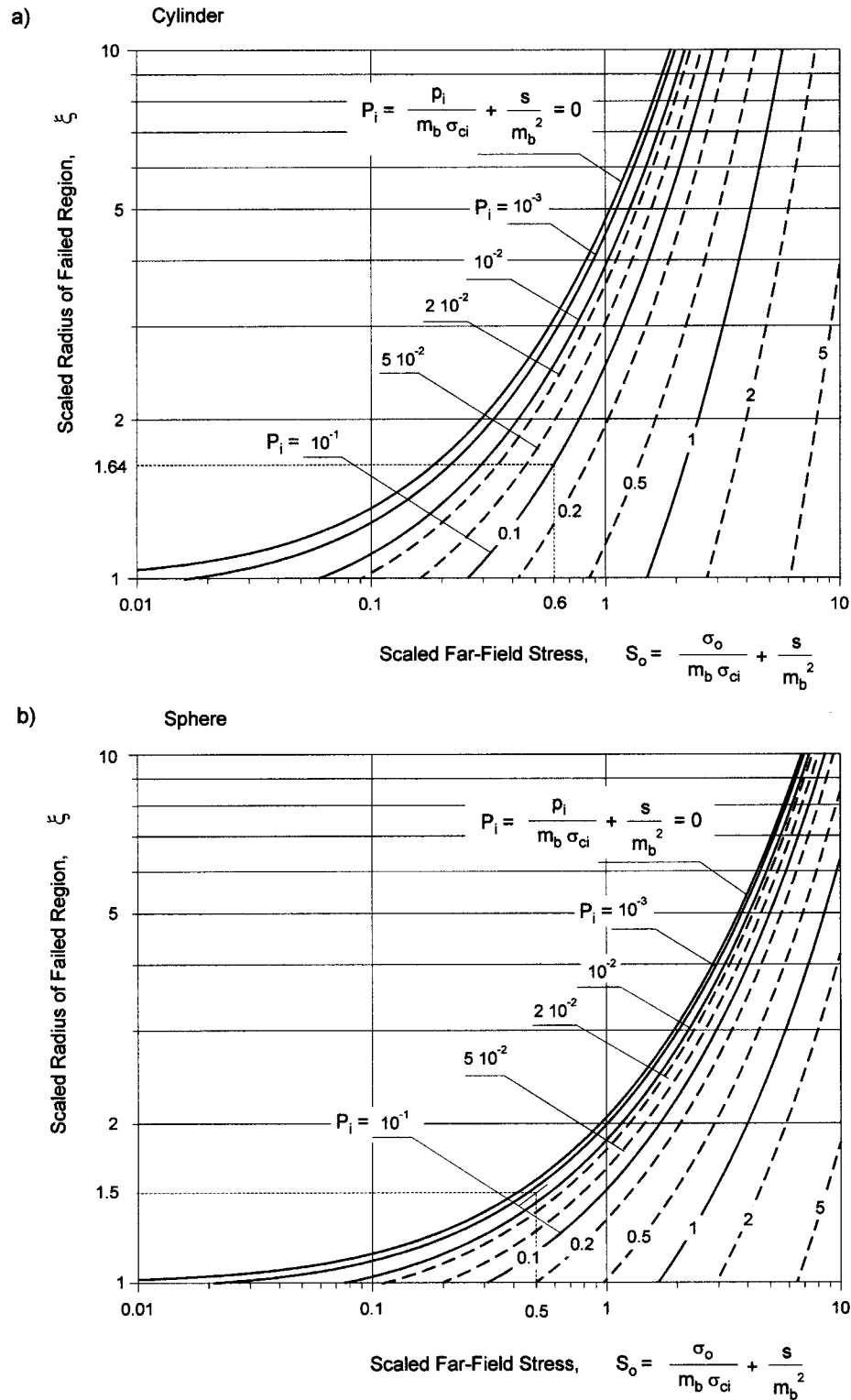$$\xi = \exp\left[\frac{2}{k}\left(\sqrt{P_i^*} - \sqrt{P_i} \right) \right] \tag{15}$$

a)

Cylinder

b)

Sphere

Fig. 8. Scaled radius of the plastic region, ξ, as a function of the scaled far-field stress, S_o, and the scaled internal pressure, P_i, for (a) cylindrical and (b) spherical openings excavated in Hoek–Brown materials. (If b is the radius of the opening, $b\xi$ is the extension of the plastic region; σ_o and p_i are the far-field stress and the internal pressure, respectively).
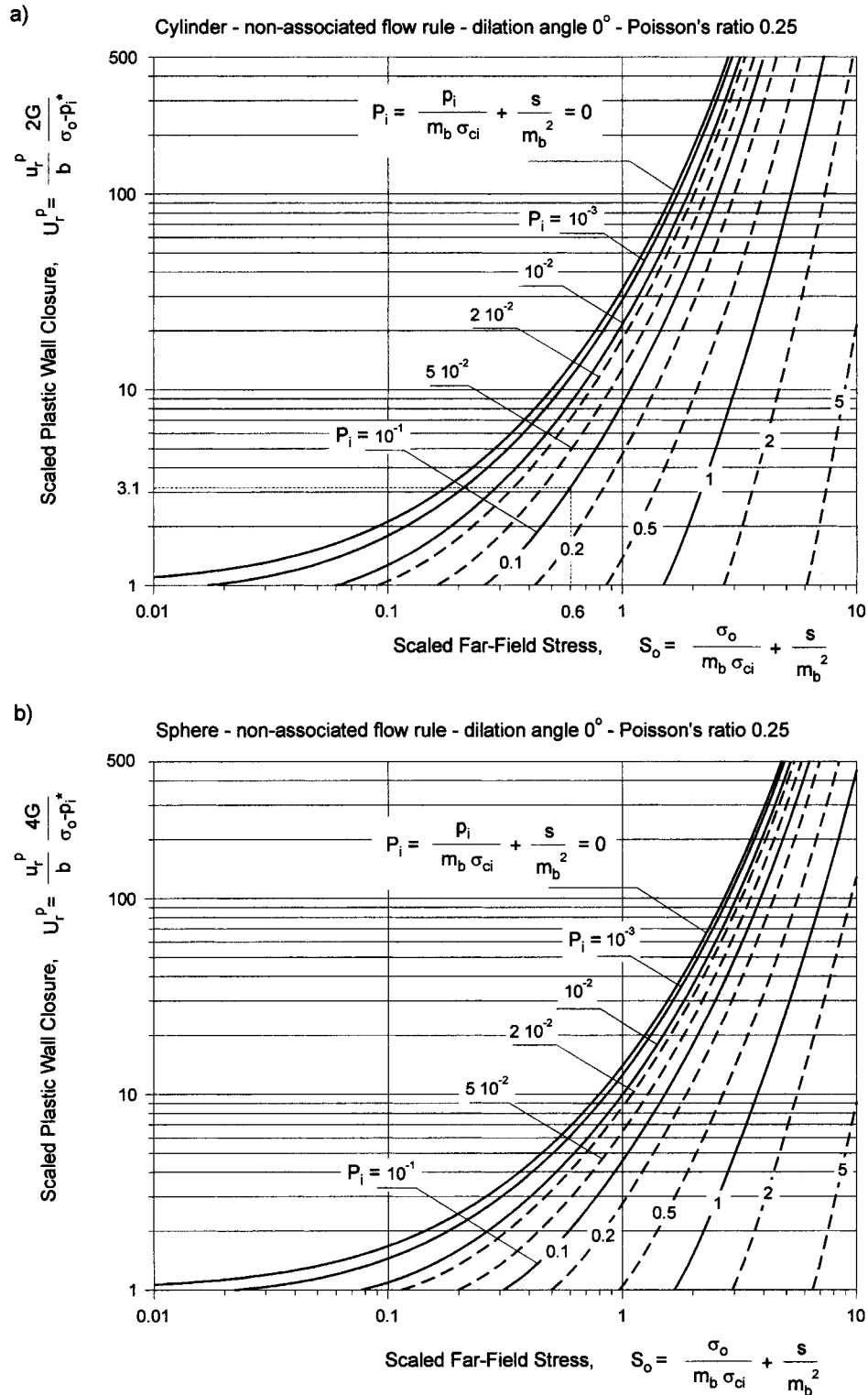
Fig. 9. Scaled wall radial displacement, U_r^p, as a function of the scaled far-field stress, S_o and the scaled internal pressure, P_i, for (a) cylindrical and (b) spherical openings. The rock mass, assumed to obey the Hoek–Brown failure criterion, has zero dilation and a Poisson's ratio equal to 0.25; b is the radius of the opening and σ_o and p_i are the far-field stress and the internal pressure, respectively.
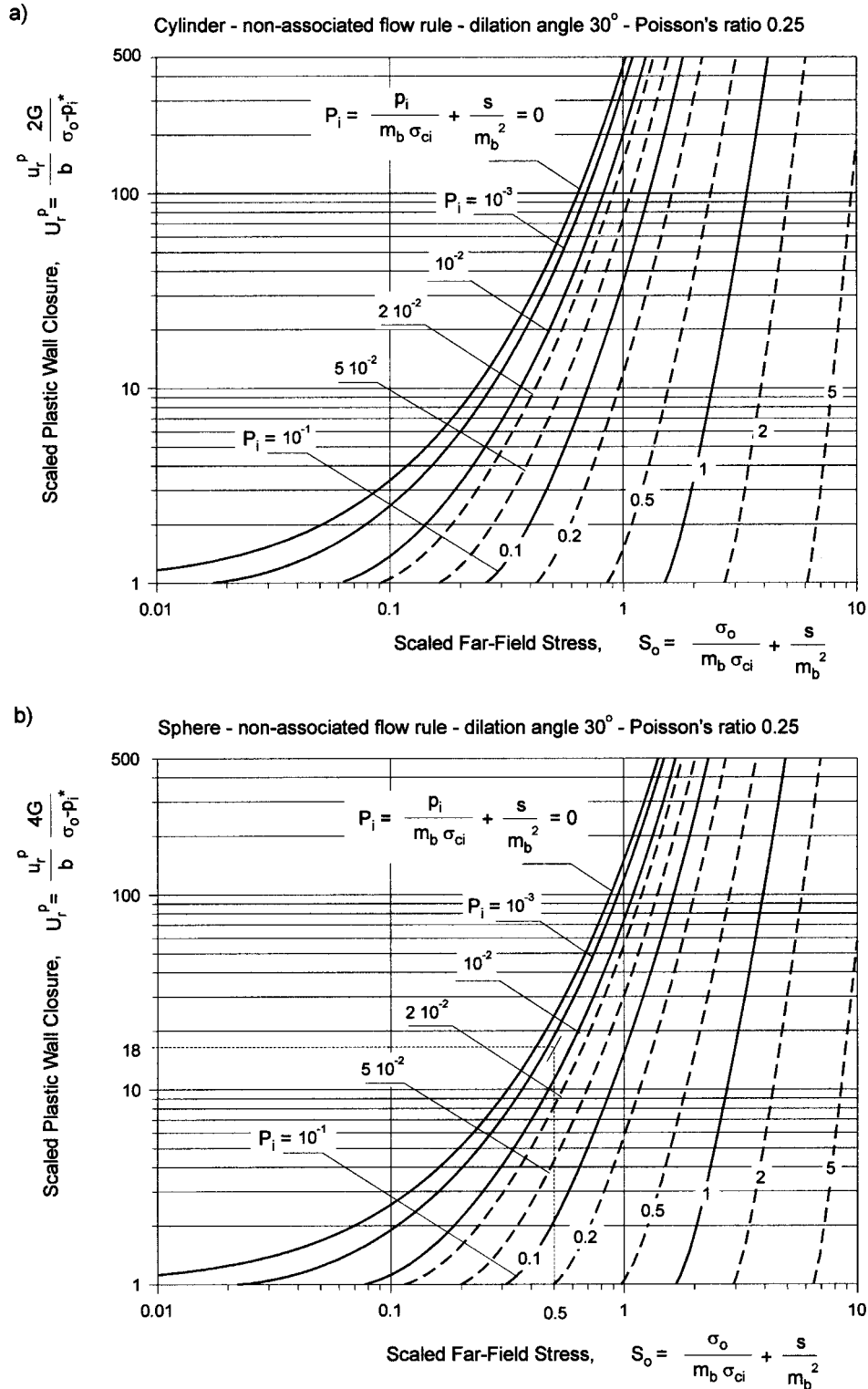
Fig. 10. Scaled wall radial displacement, U_r^p, as a function of the scaled far-field stress, S_o, and the scaled internal pressure, P_i, for (a) cylindrical and (b) spherical openings. The rock mass, assumed to obey the Hoek–Brown failure criterion, has a dilation angle equal to $30°$ and a Poisson's ratio equal to 0.25; b is the radius of the opening and σ_o and p_i are the far-field stress and the internal pressure, respectively.
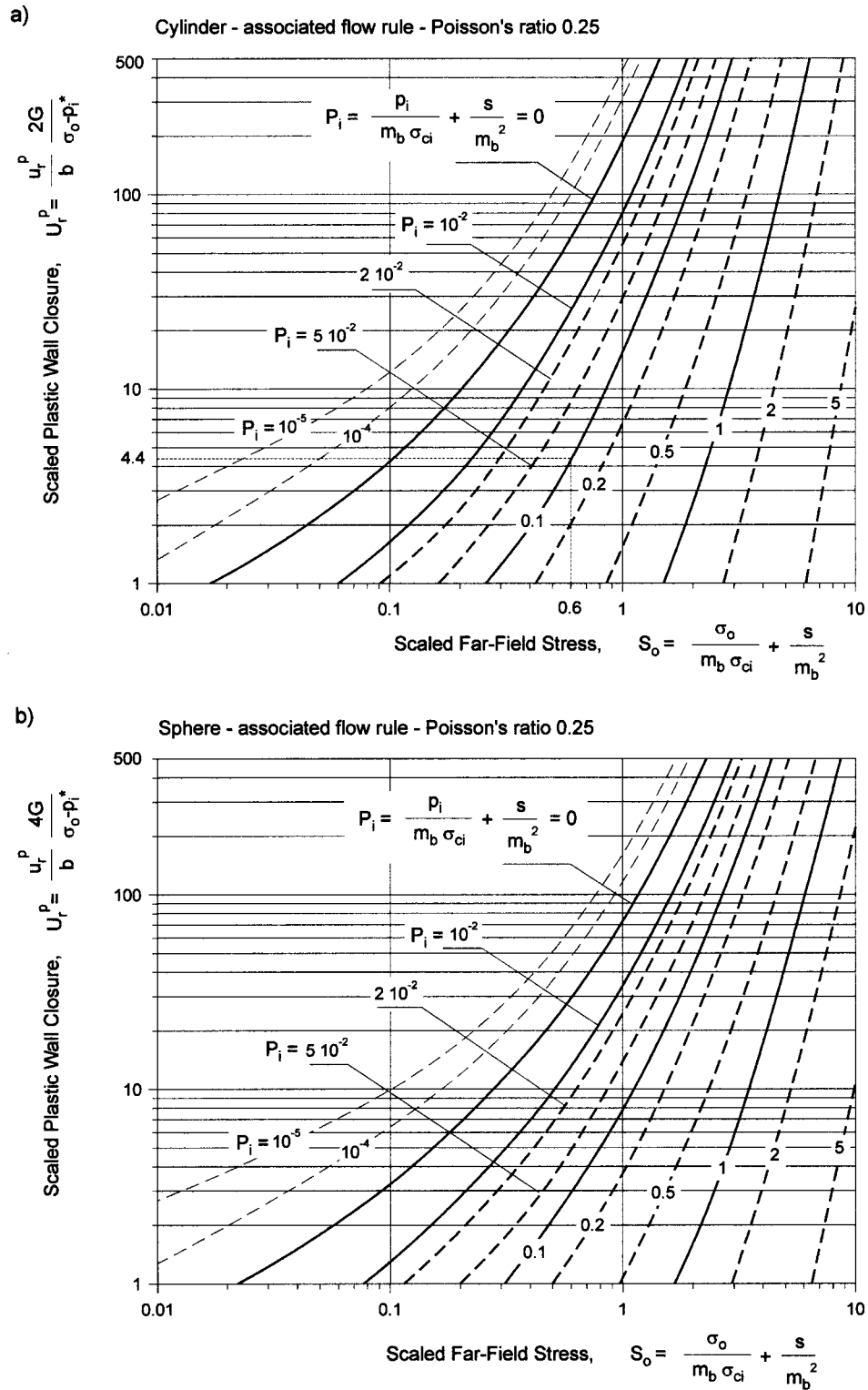
Fig. 11. Scaled wall radial displacement, U_r^p, as a function of the scaled far-field stress, S_o, and the scaled internal pressure, P_i, for (a) cylindrical and (b) spherical openings. The rock mass, assumed to obey the Hoek–Brown failure criterion and the associated flow rule; the Poisson's ratio is equal to 0.25; b is the radius of the opening and σ_o and p_i are the far-field stress and the internal pressure, respectively.

This relationship (Eq. (15)) is plotted in Fig. 8a and 8b for cylindrical and spherical openings, respectively. The horizontal axis covers the same range of values as in Fig. 6. For the vertical axis, a maximum plastic extension (ξ) equal to 10 times the radius of the opening has been chosen arbitrarily — this should certainly cover most practical cases.

Examination of Fig. 3b in conjunction with Eqs. (11) and (15) reveals an interesting practical result. As can be seen from Fig. 3b, the unconfined compressive strength of the rock mass (σ_{crm}) is zero for all GSI < 25. The practical implication of this result is that unsupported openings excavated in such poor quality materials cannot sustain any load without the development of a plastic zone around the opening. Equations (11) and (15) provide further insight on this phenomenon. Consider the case in which s is taken equal to zero (i.e. the case in which GSI = 25, according to Eq. (5)). If the cavity is unsupported (i.e. the scaled internal pressure is $P_i = 0$), the normalized extension (ξ) of the plastic region is found, by combining Eqs. (11) and (15), to be

$$\xi = \exp\left[\frac{1}{k+1}\sqrt{1 + 4\frac{\sigma_{\text{o}}}{m_b \sigma_{ci}}\left(\frac{k+1}{k}\right)^2} - \frac{1}{k+1}\right] \quad (16)$$

Equation (16) indicates that ξ will be larger than unity for *any* positive (i.e. compressive) value of far-field stress, σ_{o}. Note that, as σ_{o} tends to zero, the normalized extension ξ tends to 1.

Closed-form expressions for the stresses σ_{θ} and σ_r in the plastic region are given by Eqs. (A.58) and (A.59).

The solution for the displacement in the failed region (in particular, the convergence of the wall — i.e. the value of u_r at $r = b$), depends on the shear modulus, G, Poisson's ratio, ν, and the flow-rule considered for the inelastic deformation regime.

Figures 9 and 10 show the radial displacement of the wall for the case of a non-associated flow rule with constant dilation angle (two cases, dilation angles equal to 0 and 30°, respectively, are considered) and Poisson's ratio equal to 0.25. The graphs have been constructed using Eq. (A.38), i.e.

$$U_r^p = \xi \tilde{u}_r\left(\frac{1}{\xi}\right) \quad (17)$$

with the scaled plastic radial displacement at the wall given by

$$U_r^p = \frac{u_r^p}{b}\frac{2kG}{\sigma_{\text{o}} - p_i^*} \quad (18)$$

and the expression $\tilde{u}_r(1/\xi)$ defined by Eq. (A.66) in the Appendix — for the particular case where $\rho = 1/\xi$.

The scale of the vertical axis in these diagrams has been chosen to cover a realistic practical range. Since the magnitude $U_r^p = 1$ represents the displacement of the excavation wall when the material just reaches the elastic limit (Eq. (A.24)), the vertical coordinate indicates the size of the resulting plastic deformation as a proportion of the deformation for the (limiting) elastic case. An upper bound for the plastic wall radial displacement equal to 500 times the (maximum) elastic displacement has been chosen arbitrarily to cover all practical possibilities.

The solution for the wall radial displacement in the case of an associated flow rule and Poisson's ratio equal to 0.25 is plotted in Fig. 11a and 11b for cylindrical and spherical openings, respectively. These figures were constructed using the same relationship (Eq. (17)) above — this time with the function $\tilde{u}(\rho)$ given by the solution of Eq. (A.63), together with the coefficients (Eq. (A.69)) (Detailed discussion of this point is presented in the Appendix).

The axes in these diagrams are similar to those for the non-associated flow rule already discussed.

Figure 11 indicates that the solution for the associated flow rule is unbounded as the (scaled) internal pressure tends to zero, i.e. as $P_i \rightarrow 0$. (The basic mechanics underlying this behavior are discussed in the Appendix). The practical consequence is that such a (weak) material will tend to 'dilate' or 'flow' continuously when the scaled confining stress becomes zero. This condition can be expected at the walls of unsupported cavities in rock masses of very poor quality; in such cases, s is zero — and P_i is also zero; see Eqs. (5) and (10), respectively.

The practical consequences of this effect can be seen from the diagrams in Figs. 8 and 11. In the case of a spherical opening with a low value of S_{o} (e.g. $S_{\text{o}} \simeq 0.01$), the lower diagram in Fig. 8 indicates that the plastic region will extend only a fraction of the radius of the opening (i.e. $\xi \simeq 1$); if the scaled internal pressure is assumed to have a relatively low value (e.g. $P_i < 10^{-5}$) then, according to Fig. 11b, the radial displacement at the wall can take any value above the displacement that occurs immediately before the onset of plastic deformation (i.e. when ξ is almost unity). This suggests a disproportionate development of plastic dilation. Thus, to avoid this (unstable) case, the diagrams in Fig. 11 show curves for an (arbitrary) minimum value of $P_i = 10^{-5}$ for the scaled internal pressure (P_i).

4. Practical application of the graphical solution to spherical and cylindrical cavities

The following examples are intended to illustrate the practical application of Figs. 6–11 in determining the elasto-plastic response of cavities. Two cases are con-

a)

Data

$$S_o = \frac{\sigma_o}{m_b\,\sigma_{ci}} + \frac{s}{m_b^2} = 0.5$$

$$P_i = \frac{p_i}{m_b\,\sigma_{ci}} + \frac{s}{m_b^2} = 1.4\ 10^{-3}$$

σ_{ci} = 30 MPa
m_b = 1.7
s = 3.9 10^{-3}

(non-associated
flow rule $\psi=30°$)

G = 2.2 GPa
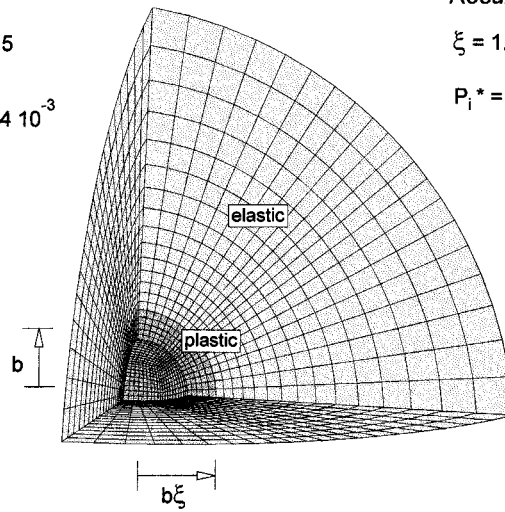ν = 0.25

Results

ξ = 1.5

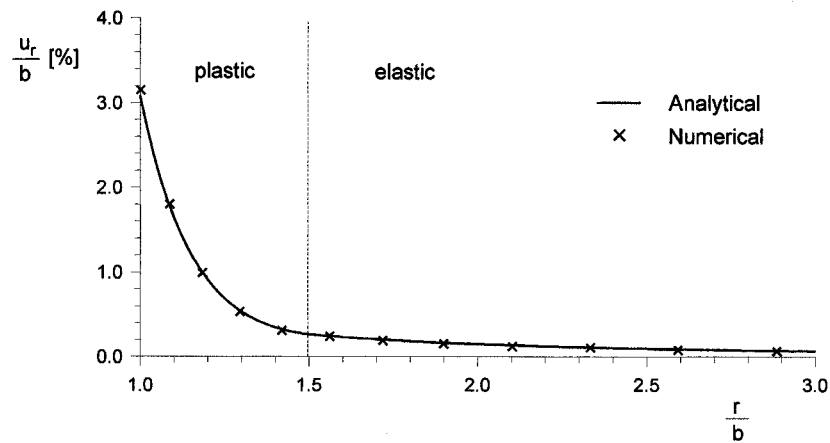$$P_i^* = \frac{p_i^*}{m_b\,\sigma_{ci}} + \frac{s}{m_b^2} = 0.20$$

(at the wall)

$$U_r^p = \frac{u_r^p}{b}\,\frac{4G}{\sigma_o - p_i^*} = 18$$

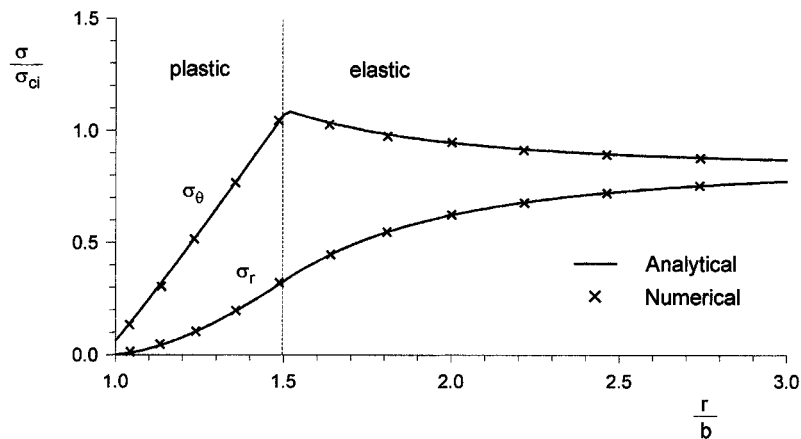$$\rightarrow\ \frac{u_r^p}{b} = 3.1\ 10^{-2}$$

b)

c)

Fig. 12. Comparison of analytical and numerical (FLAC^{3D}) solutions for a spherical cavity in a Hoek–Brown material. (a) Characteristics of the model. (b) Radial displacement and (c) radial and tangential stresses obtained in the analysis.

sidered, one for a spherical cavity, the other for a cylindrical excavation, both for a rock mass of known properties.

We will assume that an intact rock core, sampled from the rock mass and tested in the laboratory, indicates the following (intact rock) properties

$$\sigma_{ci} = 30 \text{ MPa} \quad m_i = 10 \quad E = 20 \text{ GPa} \quad v = 0.25$$

We will assume that the rock mass has been characterized as having a GSI value of 50.

With this information, the 'scaling' parameters s and m_b that account for the reduced strength of the rock mass can be read directly from the diagrams in Fig. 3. We find that

$$s = 3.9 \times 10^{-3} \quad \frac{m_b}{m_i} = 1.7 \times 10^{-1}$$

Since the value $m_i = 10$ has been found from the laboratory tests, $m_b = 1.7$.

4.1. Rock mass deformability

Just as the strength of the rock mass is usually lower than the strength of the intact rock, so, too, the (elastic) deformation modulus of the rock mass is usually lower than that of the intact rock. Serafim and Pereira [33] have proposed an empirical relationship to compute the deformation modulus of the rock mass from the unconfined compressive strength of an intact rock sample and the value of the rock mass rating (RMR) by Bieniawski [3]. Based on the original equation by Serafim and Pereira, Hoek and Brown [17] have proposed the following relationship between the rock mass modulus (E_{rm}) and the GSI

$$E_{rm} = \sqrt{\frac{\sigma_{ci}}{100}} 10^{\frac{GSI-10}{40}} \qquad (19)$$

For the rock mass considered in this example (GSI = 50 and σ_{ci} = 30 MPa), Eq. (19) indicates a value of E_{rm} = 5.5 GPa. In the equations presented earlier in this section, the shear modulus, G, was used, rather than the deformation modulus, E. The shear modulus for the rock mass, G_{rm}, can be estimated from the modulus E_{rm} using the classic relationship from isotropic elasticity,

$$G_{rm} = \frac{E_{rm}}{2(1+v)} \qquad (20)$$

For E_{rm} = 5.5 GPa and v = 0.25, we obtain G_{rm} = 2.2 GPa.

4.2. Elasto-plastic deformation around an unsupported spherical cavity

Having determined the appropriate rock mass properties, we can now calculate the response of the rock to the loads induced by formation of the cavity.

We consider first a spherical cavity of radius b = 10 m created in a rock mass having the mechanical properties described above. The far-field stress is assumed to be σ_o = 25 MPa and the cavity is unsupported, i.e. the internal pressure, p_i, is equal to zero. We will also assume the rock mass to obey a non-associated flow rule with a dilation angle ψ equal to 30°.

The scaled far-field stresses and internal pressure (S_o and P_i respectively) needed in the diagrams are, then,

$$S_o = \frac{\sigma_o}{m_b \sigma_{ci}} + \frac{s}{m_b^2} = 0.5$$

$$P_i = \frac{p_i}{m_b \sigma_{ci}} + \frac{s}{m_b^2} = 1.4 \times 10^{-3}$$

The scaled critical internal pressure (P_i^*) for which the elastic limit of the rock mass is reached (i.e. below which a plastic region will develop) can now be read from Fig. 6, i.e.

$$P_i^* = \frac{p_i^*}{m_b \sigma_{ci}} + \frac{s}{m_b^2} = 0.20$$

From this expression, the critical internal pressure is found to be p_i^* = 10 MPa. Thus, since the internal pressure assumed for the cavity is zero, a plastic region will develop uniformly around the cavity.

The normalized extension of this plastic region can be read from the lower diagram in Fig. 8,

$$\xi = 1.5$$

Since the cavity has a radius b = 10 m, the actual radius of the elasto-plastic interface will be $b\xi$ = 15 m.

For a non-associated flow rule with dilation angle equal to 30°, the normalized radial displacement at the wall of the cavity (U_r^p) can be read from the lower diagram in Fig. 10,

$$U_r^p = \frac{u_r^p}{b} \frac{4G}{\sigma_o - p_i^*} = 18$$

With the scaling constants already defined, the radial displacement is found to be u_r^p = 0.31 m.

The results obtained for this example are summarized in Fig. 12a.

As a check on the results, a numerical analysis was carried out using the finite difference code FLAC[3D] [22] for the same geometrical and mechanical properties. Fig. 12b shows the distribution of radial displacements as a function of distance from the center of the (spherical) cavity. The analytical solution is computed

a)

Data

$$S_o = \frac{\sigma_o}{m_b\,\sigma_{ci}} + \frac{s}{m_b^2} = 0.6$$

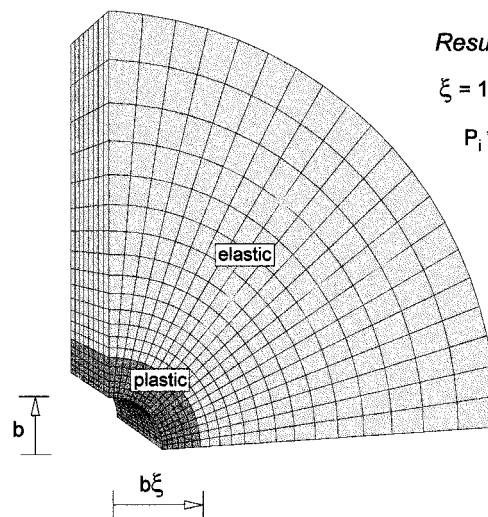$$P_i = \frac{p_i}{m_b\,\sigma_{ci}} + \frac{s}{m_b^2} = 0.1$$

$\sigma_{ci} = 30$ MPa
$m_b = 1.7$
$s = 3.9 \; 10^{-3}$

(associated flow rule)

$G = 2.2$ GPa
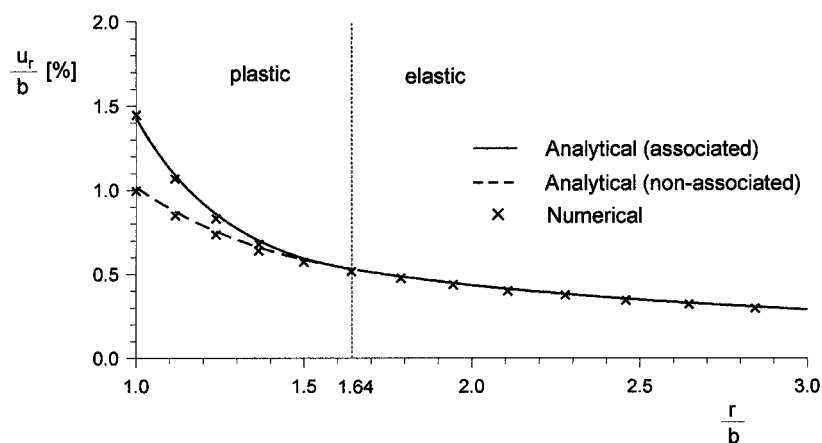$\nu = 0.25$

elastic

plastic

b

bξ

Results

$\xi = 1.64$

$$P_i^* = \frac{p_i^*}{m_b\,\sigma_{ci}} + \frac{s}{m_b^2} = 0.32$$

$$U_r^p = \frac{u_r^p}{b} \frac{4G}{\sigma_o - p_i^*} = 4.4$$

$$\rightarrow \frac{u_r^p}{b} = 1.4\;10^{-2}$$

b)

$\frac{u_r}{b}$ [%]

plastic   elastic

—— Analytical (associated)
- - - Analytical (non-associated)
×   Numerical

$\frac{r}{b}$

c)

$\frac{\sigma}{\sigma_{ci}}$

plastic   elastic

σ_θ

σ_r

—— Analytical
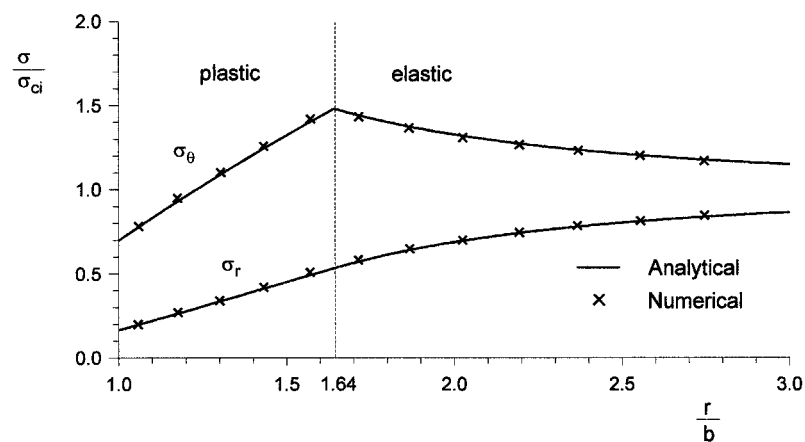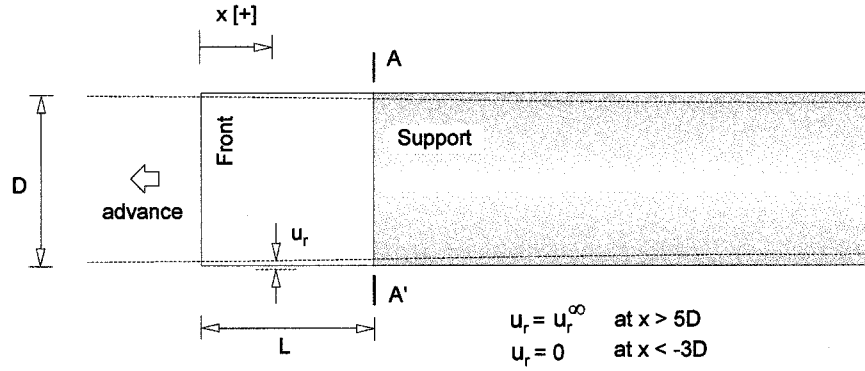×   Numerical

$\frac{r}{b}$

Fig. 13. Comparison of analytical and numerical (FLAC^{3D}) solutions for a cylindrical cavity in a Hoek–Brown material. (a) Characteristics of the model. (b) Radial displacement and (c) radial and tangential stresses obtained in the analysis.
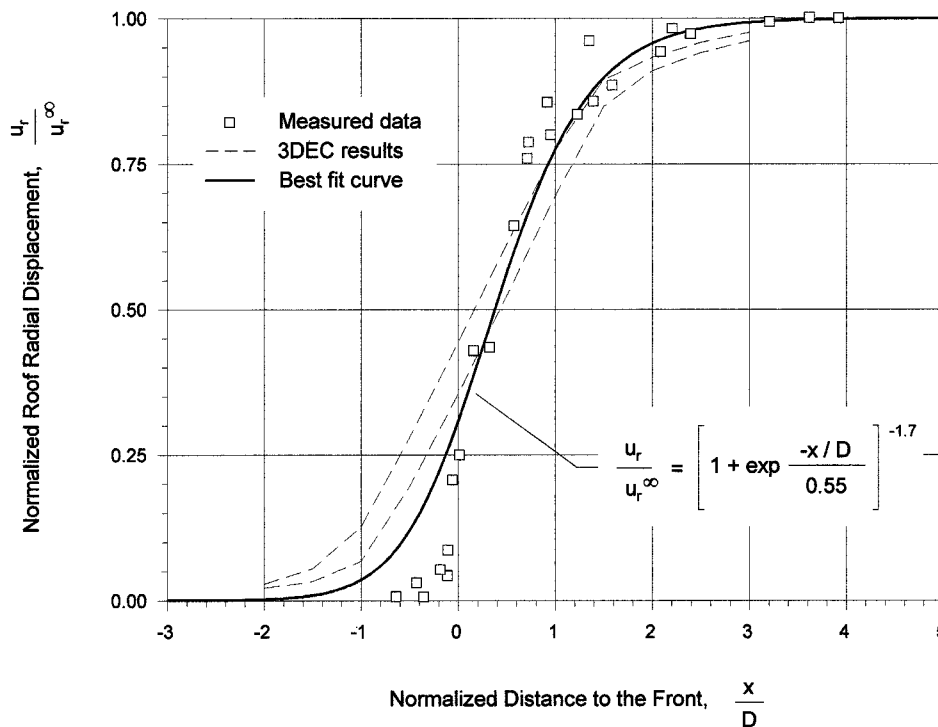
a)

b)

Fig. 14. (a) Schematic representation of radial displacements in the vicinity of the face in a long cylindrical tunnel. (b) Radial displacements (normalized with respect to the final wall closure) versus normalized distance to the front. The squares represent extensometer measurements in the roof of a tunnel at the Mingtam Power Cavern project while the dashed curves represent the upper and lower bounds of results obtained with 3DEC [7,23]. The solid line is a best fit to the measured data and numerical results [21].

using Eq. (A.66) in the Appendix. The distribution of radial and tangential stresses are shown in Fig. 12c. (The analytical solution is given by Eqs. (A.58) and (A.59)). As can be seen, there is good agreement between the analytical solution and the FLAC^{3D} solution.

4.3. Elasto-plastic deformation around a supported cylindrical cavity

The second example considers a supported cylindri-

cal cavity of radius $b = 5$ m excavated in a rock mass with the same properties as in the previous example. In this case, the far-field stress is assumed to be $\sigma_o = 30$ MPa and the internal pressure is $p_i = 5$ MPa. Two situations are examined: one in which the rock mass obeys an associated flow-rule and another in which it obeys a non-associated flow-rule, where there is no dilation (i.e. $\psi = 0°$).

For the given data, the scaled far-field stresses and internal pressure are

a)

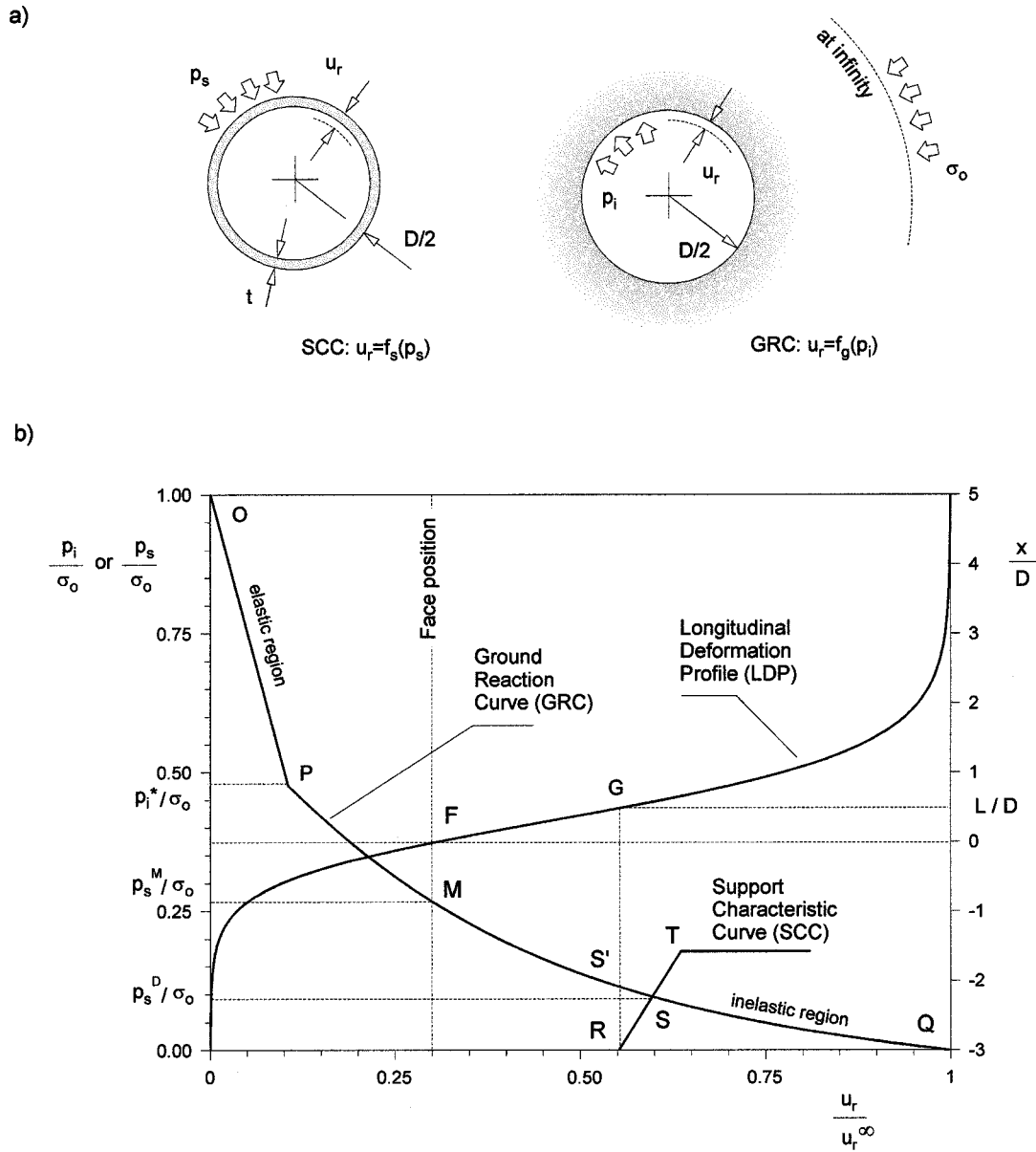SCC: $u_r = f_s(p_s)$ GRC: $u_r = f_g(p_i)$

b)

Fig. 15. (a) Schematic representation of a section of a closed circular lining and a circular tunnel used in the definitions of Support Characteristic Curve (SCC) and Ground Reaction Curve (GRC) respectively. (b) Dimensionless representation of SCC, GRC and Longitudinal Deformation Profile (LDP).

$$S_o = \frac{\sigma_o}{m_b \sigma_{ci}} + \frac{s}{m_b^2} = 0.6 \quad P_i = \frac{p_i}{m_b \sigma_{ci}} + \frac{s}{m_b^2} = 0.1$$

The scaled critical internal pressure (P_i^*) at which the elastic limit of the rock mass is reached, can be read from Fig. 6

$$P_i^* = \frac{p_i^*}{m_b \sigma_{ci}} + \frac{s}{m_b^2} = 0.32$$

From this expression, the critical internal pressure is found to be $p_i^* = 16$ MPa. Since the internal pressure is assumed to be 5 MPa, a plastic region will develop around the cavity.

The normalized extension (ξ) of this plastic region is read from the upper diagram in Fig. 8 and is found to be

$$\xi = 1.64$$

Since the cavity has a radius $b = 5$ m, this indicates that the radius of the elastoplastic interface will be $b\xi = 8.2$ m.

For the associated flow rule, the normalized radial displacement at the wall of the cavity can be read from the upper diagram in Fig. 11,

$$U_r^p = \frac{u_r^p}{b} \frac{2G}{\sigma_o - p_i^*} = 4.4$$

For the scaling constants already defined, the resulting radial displacement is found to be $u_r^p = 0.07$ m.

In the case of the non-associated flow rule, the normalized radial displacement, U_r^p, is read from the upper diagram in Fig. 9; for the value obtained (i.e. $U_r^p = 3.1$), the radial displacement is $u_r^p = 0.05$ m.

The results for this example are summarized in Fig. 13a. A FLAC^{3D} model was again run to compare results. Fig. 13b shows the distribution of radial displacements as a function of the distance to the center (computed as in Fig. 12b), while Fig. 13c shows the distribution of radial and tangential stresses. Again, good agreement is found between the analytical expressions and the results given by FLAC^{3D}.

4.3.1. Determination of ground reaction curves for cylindrical tunnels — for use in the Convergence–Confinement Method of Support Design

The Convergence–Confinement procedure is a method of calculating the load imposed on a support installed behind the face (or front) of the tunnel. When a section of lining is installed in the vicinity of the tunnel face, some part of the load redistributed around the excavation is carried by the face. As the face advances (i.e. away from the installed support), the 'face effect' decreases and the support must carry a greater proportion of the load that the face had carried earlier. When the face has moved well away from the section, the support must carry, effectively, the full design load.

A detailed treatment of the convergence–confinement concept can be found in Panet [31]. Only a brief outline will be presented here. Application of the solution presented in Section 3 to construction of the socalled 'ground reaction curves' will then be addressed in some detail.

Consider the situation shown in Fig. 14a. A cylindrical tunnel of diameter D is excavated at depth in a rock mass and is subject to a hydrostatic stress field σ_o. The tunnel face, defined by the coordinate $x = 0$, is advancing towards the left of the tunnel. We will consider a support installed at a section $A–A'$ along the tunnel, located at a distance L from the face. The goal is to find the final pressure p_s^D that the rock mass will transmit to the support once the tunnel has advanced sufficiently for the supporting effect of the face to have disappeared. All deformations are assumed to occur in a plane perpendicular to the axis of the tunnel (i.e. the problem is two dimensional plane strain). Radial displacements are also assumed to be uniform (i.e. independent of angular position around the excavation).

The three basic components of the convergence–confinement method are, then, the longitudinal deformation profile (LDP), the support characteristic curve (SCC) and the ground reaction curve (GRC).

The LDP is the graphical representation of radial displacements occurring along the axis of the tunnel — for sections located ahead and behind the face. Fig. 14b shows such a profile. The horizontal axis represents the distance to the face, normalized with respect to the tunnel diameter (Fig. 14(b)). The vertical axis represents the corresponding radial displacement, u_r, normalized with respect to the final radial displacement u_r^∞ (this corresponds to the convergence in an unsupported infinitely long tunnel where there is no 'face effect'). The squares in the diagram represent measurements obtained from extensometers in the roof of a tunnel at the Mingtam Power Cavern project, while the dashed lines represent lower and upper bounds of results obtained with the numerical code 3DEC [7,23]. The solid line is a best fit to the measured data and results from numerical models (Hoek [21]). Figure 14b indicates that, for sections located approximately three diameters ahead of the face, the radial displacement is zero (i.e. there is no effect of the approaching tunnel). Similarly, for sections located approximately five diameters behind the face, the maximum possible displacement has occurred (i.e. there is no longer a support contribution from the face).

Consider now the sketch on the left of Fig. 15a. This represents a section of an annular lining, thickness t, to be installed in the tunnel, diameter D. A p_s imposed by the rock mass on the lining produces a radial displacement u_r. The SCC is defined simply as the relationship between the increasing pressure p_s and the increasing radial displacement u_r. The relationship depends on the geometrical and mechanical characteristics of the support. Brady and Brown [4] give equations defining the SCC for several types of linings (Fig. 15b shows a SCC for a support that is designed to yield — i.e. slip, after a load represented by point T is reached).

The sketch on the right side of Fig. 15a represents a section along the axis of the tunnel. Here p_i represents the internal pressure provided by the support and u_r the corresponding radial displacement of the support-rock interface. The GRC is defined as the relationship between the decreasing pressure p_i and the increasing radial displacement u_r. The relationship depends on the mechanical properties of the rock mass and can be obtained from elasto-plastic solutions, such as the one presented in Section 3. This will be discussed later in detail.

The LDP, SCC and GRC can all be plotted on a single diagram, as shown in Fig. 15b. Here, the horizontal axis represents the radial displacement u_r at a given section along the tunnel — normalized with

respect to the final radial displacement u_r^∞. The left vertical axis represents the pressure p_i or p_s — acting on the tunnel walls and support respectively, normalized with respect to the far-field stress σ_o (Fig. 15a); the right vertical axis represents the normalized distance x/D from a section of the tunnel to the face (Fig. 14a).

In this reference system, the LDP is the same curve as shown in Fig. 14b, but rotated clockwise 90 degrees and 'inverted' about the vertical axis in Fig. 14b. The GRC extends from point O corresponding to zero deformation (at $x/D < -3$) to point Q corresponding to the final deformation (at $x/D > 5$). P represents the point of transition between elastic and plastic displacements (defined by the pressure p_i^* discussed in Section 3).

The SCC extends from point R defined by the relative distance L/D of the section to the face (Fig. 14a) to point T defined by the limiting pressure that makes the support yield. Note that point R is directly below point G (coordinate L/D in the vertical axis on the right).

During the time that the support is being installed, stability is maintained by the supporting effect of the face. Thus, the vertical segment RS' represents the normalized pressure being taken by the face at the moment that the support is installed. As the face advances, both the support and excavation start deforming by the same amount — with the pressure p_s on the support increasing and the confining effect p_i on the periphery of the tunnel decreasing. In the limit, when the supporting effect of the face has disappeared, the system reaches equilibrium at point S, i.e. the intersection of the GRC and the SCC. The pressure p_s^D defined by point S represents the final pressure (or design load) that the rock will transmit to the support. These curves show clearly that the support will not be subject to a pressure larger than p_s^M — defined by point M (this pressure would be achieved only in the hypothetical case of an infinitely rigid support installed at the face itself; i.e. for the case of a vertical SCC, starting at the base of the line referred to as 'face position'). On the other hand, a support will not take any load if placed at point Q, since the maximum convergence has occurred already.

The solution for cylindrical cavities presented in section 3 assumes a monotonic reduction of internal pressure, p_i, from the initial far-field stress value, σ_o. This can be applied conveniently to the construction of Ground Reaction Curves for rock masses obeying the Hoek–Brown failure criterion. Consider a cylindrical tunnel of diameter D, subject to hydrostatic far-field stresses, σ_o and internal pressure, p_i (Fig. 5a). Properties of the intact rock are defined by parameters σ_{ci} and m_i. As shown in the earlier examples in Section 4, the geological strength index allows the remaining

properties of the rock mass to be defined; i.e. the parameters m_b, s and the shear modulus G_{rm} — for a given value of Poisson's ratio v.

The scaled values of far-field stress, S_o and internal pressure, P_i, can then be computed using Eq. (10).

For a cylindrical cavity, the scaled critical internal pressure, P_i^*, below which plastic development occurs, is defined (from Eq. 11) as,

$$P_i^* = \frac{1}{16}\left[1 - \sqrt{1 + 16S_o}\right]^2 \tag{21}$$

Applying the inverse of the transformation (Eq. (10)), the actual critical internal pressure, p_i^*, (i.e. the vertical coordinate of point P in Fig. 15a) is given by,

$$p_i^* = \left[P_i^* - \frac{s}{m_b^2}\right]m_b\sigma_{ci} \tag{22}$$

For values of internal pressure above the critical pressure p_i^* (i.e. $p_i > p_i^*$), the rock mass remains in the elastic state. The relationship between the radial displacements (u_r^e) and internal pressure (p_i) in the elastic part of the GRC (i.e. segment OP in Fig. 15b) is given [see Eqs. (13) and (14)] by the expression

$$u_r^e = \frac{\sigma_o - p_i}{4G_{rm}}D \tag{23}$$

For values of internal pressure $p_i < p_i^*$, a plastic region develops around the opening. The normalized extent of this zone [see Eq. (15)] is,

$$\xi = \exp\left[2\left(\sqrt{P_i^*} - \sqrt{P_i}\right)\right] \tag{24}$$

Considering a non-associated flow rule characterized by a dilation coefficient K_p^*, computed from the dilation angle, ψ, according to the expression $K_p^* = [1 + \sin\psi]/[1 - \sin\psi]$, the relationship between the radial displacement and internal pressure in the plastic part of the GRC (i.e. the segment PQ in Fig. 15b), is given by Eq. (A.66) in the Appendix — rewritten here as Eq. (25),

$$\begin{aligned}
\frac{u_r^p}{D}\frac{4G_{rm}}{\sigma_o - p_i^*} = {} & \frac{K_p^* - 1}{K_p^* + 1} + \frac{2}{K_p^* + 1}\xi^{K_p^* + 1} \\
& + \frac{1 - 2v}{4(S_o - P_i^*)}(\ln\xi)^2 \\
& - \left[\frac{1 - 2v}{K_p^* + 1}\frac{\sqrt{P_i^*}}{S_o - P_i^*}\right. \\
& \left. + \frac{1 - v}{2}\frac{K_p^* - 1}{(K_p^* + 1)^2}\frac{1}{S_o - P_i^*}\right] \\
& \times \left[(K_p^* + 1)\ln\xi - \xi^{K_p^* + 1} + 1\right]
\end{aligned} \tag{25}$$

For the case of non-dilating material (i.e. $K_p^* = 1$), Eq. (25) takes the form,
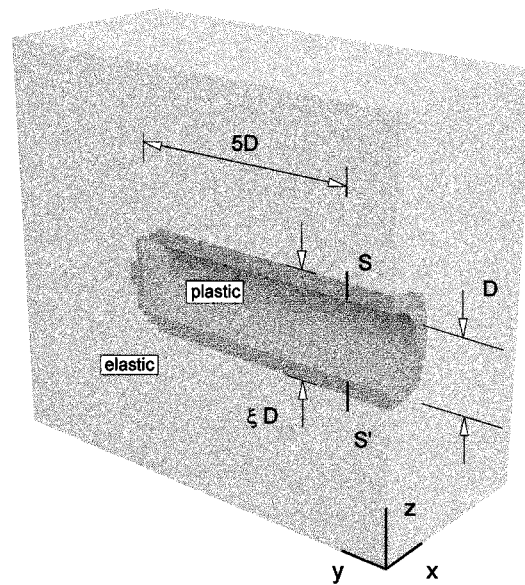
a)

Data

D = 10 m
σ_o = 10 MPa
σ_{ci} = 30 MPa
m_i = 10
ν = 0.25
ψ = 0° (non-associated flow rule)

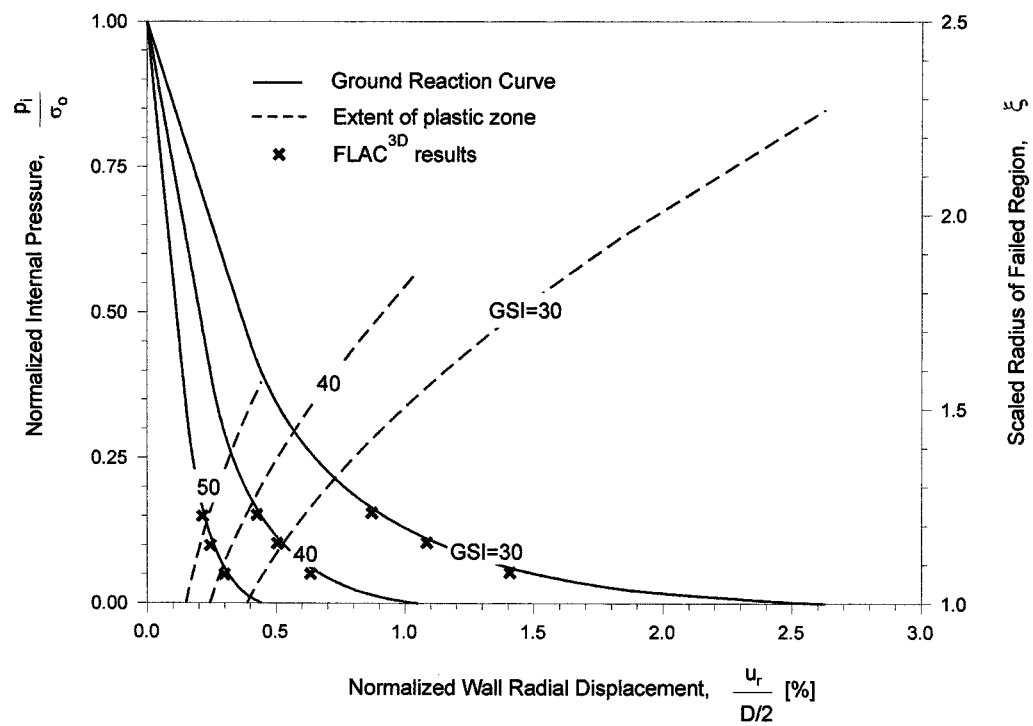| GSI	m_b	s	G_{rm} (GPa)
50	1.7	$3.9\ 10^{-3}$	2.2
40	1.2	$1.3\ 10^{-3}$	1.2
30	0.8	$0.4\ 10^{-3}$	0.7

b)

Fig. 16. (a) Analysis of convergence and extent of plastic behavior for a section of tunnel in the vicinity of the tunnel face. (b) Ground Reaction Curve and normalized plastic extent for section SS′ in the model. The dots in the diagram correspond to results obtained with FLAC^{3D}.

$$\frac{u_r^p}{D}\frac{4G_{\rm rm}}{\sigma_{\rm o}-p_{\rm i}^*} = \left[\frac{1-2\nu}{2}\frac{\sqrt{P_{\rm i}^*}}{S_{\rm o}-P_{\rm i}^*}+1\right]\xi^2$$
$$+\frac{1-2\nu}{4(S_{\rm o}-P_{\rm i}^*)}\ln(\xi)^2$$
$$-\frac{1-2\nu}{2}\frac{\sqrt{P_{\rm i}^*}}{S_{\rm o}-P_{\rm i}^*}[2\ln(\xi)+1] \tag{26}$$

The correctness of Eqs. (22), (24) and (26) can be verified by transforming the Hoek–Brown parabola into a linear yield envelope for which a solution already exists. Such a transformation is obtained, for example, by making the parameter $m_{\rm b}$ in Eq. (2) tend to zero. In such a case, the Hoek–Brown yield condition transforms into the Mohr–Coulomb failure criterion for zero friction angle and unconfined compressive strength, $\sigma_{\rm crm}$ (Eq. (6)). Material obeying this particular yield condition is also known as Tresca material, with the cohesion being $(1/2)\sigma_{\rm crm}$. The relationship between the principal stresses then becomes

$$\sigma_1 = \sigma_3 + \sigma_{\rm crm} \tag{27}$$

The limit of Eqs. (22), (24) and (26) as $m_{\rm b}$ tends to zero is evaluated using l'Hopital's rule.

The critical internal pressure, $p_{\rm i}^*$, is then found to be,

$$\lim_{m_{\rm b}\to 0} p_{\rm i}^* = \sigma_{\rm o} - \frac{1}{2}\sigma_{\rm crm} \tag{28}$$

and the normalized extent, ξ,

$$\lim_{m_{\rm b}\to 0} \xi = \exp\left[\frac{\sigma_{\rm o}-p_{\rm i}}{\sigma_{\rm crm}}-\frac{1}{2}\right] \tag{29}$$

and the wall radial displacement, u_r^p, is

$$\lim_{m_{\rm b}\to 0}\frac{u_r^p}{D}\frac{4G_{\rm rm}}{\sigma_{\rm o}-p_{\rm i}^*} = 2(1-\nu)\xi^2 - (1-2\nu)[2\ln(\xi)+1] \tag{30}$$

Equations (28)–(30) above are the classical expressions normally used in practice for the particular case of frictionless non-dilating material (for example, Duncan Fama [12] and Hoek et al. [19]).

To illustrate the construction of Ground Reaction Curves using Eqs. (22)–(26) we will consider the case of an unsupported section of tunnel of diameter D in the vicinity of the face (as shown in Fig. 16a). We wish to determine the extent of the plastic region and the convergence as the internal pressure is reduced from the (initial) in situ stress value towards zero — for a section located five diameters behind the face (section SS' in the figure). In this particular example, the diameter of the tunnel is $D = 5$ m, the initial stress field is $\sigma_{\rm o} = 10$ MPa and the properties of the intact material are $\sigma_{\rm ci} = 30$ MPa and $m_{\rm i} = 10$. Rock masses of decreasing qualities, characterized by GSI values equal

to 50, 40 and 30, are considered. The elastic properties are computed with Eqs. (19) and (20) assuming a Poisson's ratio $\nu = 0.25$ (the resulting properties are summarized in Fig. 16a).

The ground reaction curves constructed using Eqs. (21)–(26) are shown in Fig. 16b (note that alternatively, the results can be obtained graphically by means of the diagrams in Figs. 6–11). Curves representing the normalized extent, ξ, of the plastic region are also included in the diagram (the value is read on the vertical axis located on the right side of the diagram). FLAC$^{\rm 3D}$ models were set up and solved for the lower range of internal pressures: values of $p_{\rm i} = 0.5$, 1.0 and 1.5 MPa; the results of these models are shown as crosses in the diagrams. Good agreement is found between the analytical solution proposed in this paper and results obtained from the numerical models.

4.3.2. Case study. Analysis of the stability of underground cavities left by underground test explosions at Mururoa and Fangataufa

An underground nuclear explosion leads to the rapid formation (within one-tenth of a second) of a large spherical cavity of radius $R_{\rm c}$. The shock wave generated by the detonation produces intense damage of the rock mass up to a distance of approximately $5R_{\rm c}$. Some hours or days later, the roof above the cavity collapses, leading to the formation of a 'chimney' of more or less finely broken rock of height $H_{\rm c}$. Measurements indicate that the chimneys may vary in height from approximately $5R_{\rm c}$ for small explosions to a maximum of $8R_{\rm c}$ for the largest explosions (i.e. $H_{\rm c} = 5R_{\rm c} \backsim 8R_{\rm c}$) above the detonation point. This suggests that the broken rock resulting from the chimney collapse has an overall or 'bulk' density approximately $30 \backsim 18\%$ less than the rock in place before the explosion (i.e. the rubble contains $30 \backsim 18\%$ void space).

The International Geomechanical Commission (IGC) was established at the request of the French Government in 1995 as an independent group to assess the long term effects of underground nuclear tests carried out by France since 1966 on the structural stability and hydrology of the atolls of Mururoa and Fangataufa in French Polynesia. One of the tasks of this commission was to analyze the stability of cavities created by the explosions and to quantify the damage induced at the ground surface (Fairhurst et al. [13]).

Most of the tests in the atolls were carried out in volcanic formations (basalts) at depths between 500 and 1000 m from the surface. The volcanics were overlain by carbonate formations (limestones and dolomites) that extend to depths of the order of 500 m from the surface.
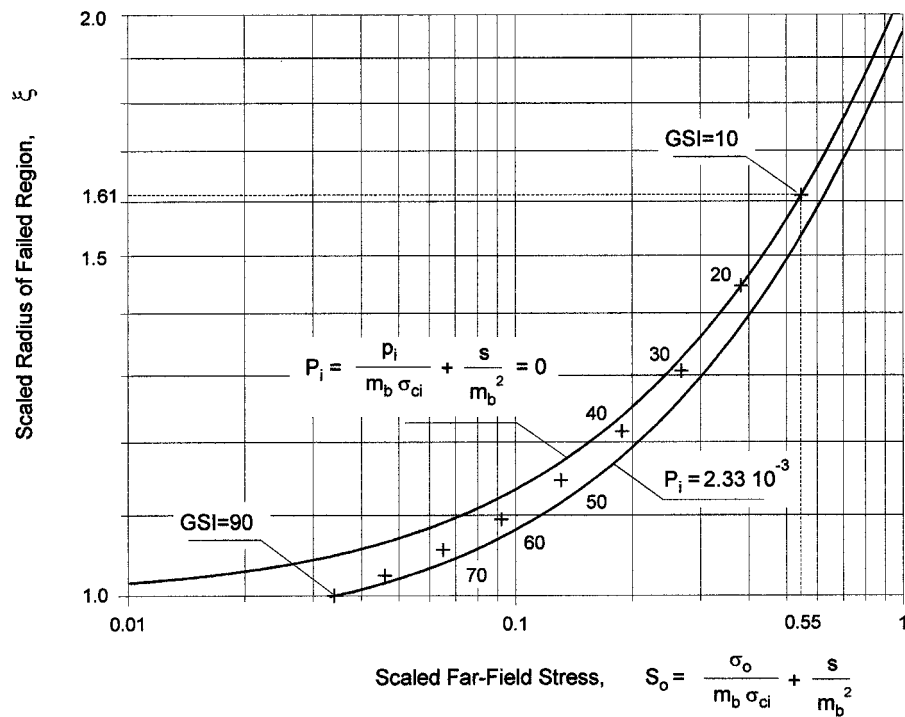
a)
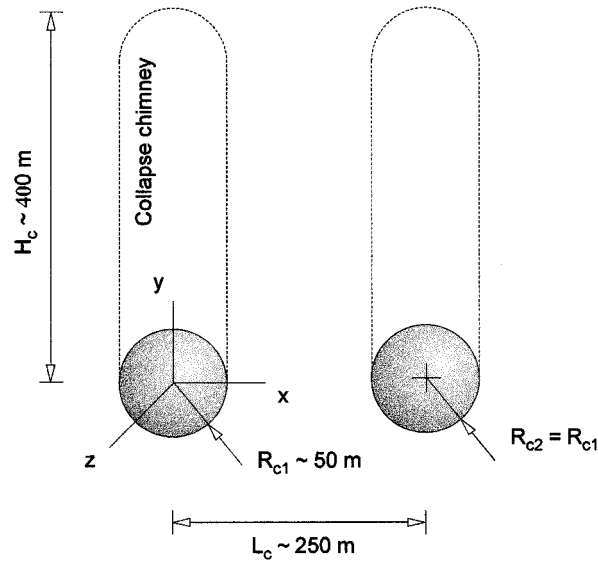
b)

Fig. 17. (a) Schematic representation of two neighboring cavities created by underground nuclear test explosions. (b) Normalized extension of the damaged region around a spherical cavity for GSI values between 10 and 100 ($\sigma_{ci} = 75$ MPa, $m_i = 17$ and $\sigma_o = 28$ MPa assumed).

Earlier underground tests at the Nevada Test Site (USA), in volcanic tuff, had resulted in chimney formation that extended continuously from the explosion cavity to the surface — forming a surface subsidence crater. French officials maintained that this continuous col-

lapse did not develop in tests on the atolls, but that a zone of undamaged volcanic and carbonate rock separated and isolated the surface from the underground cavities.

The possibility that two explosions detonated in close proximity to each other (at different times) could
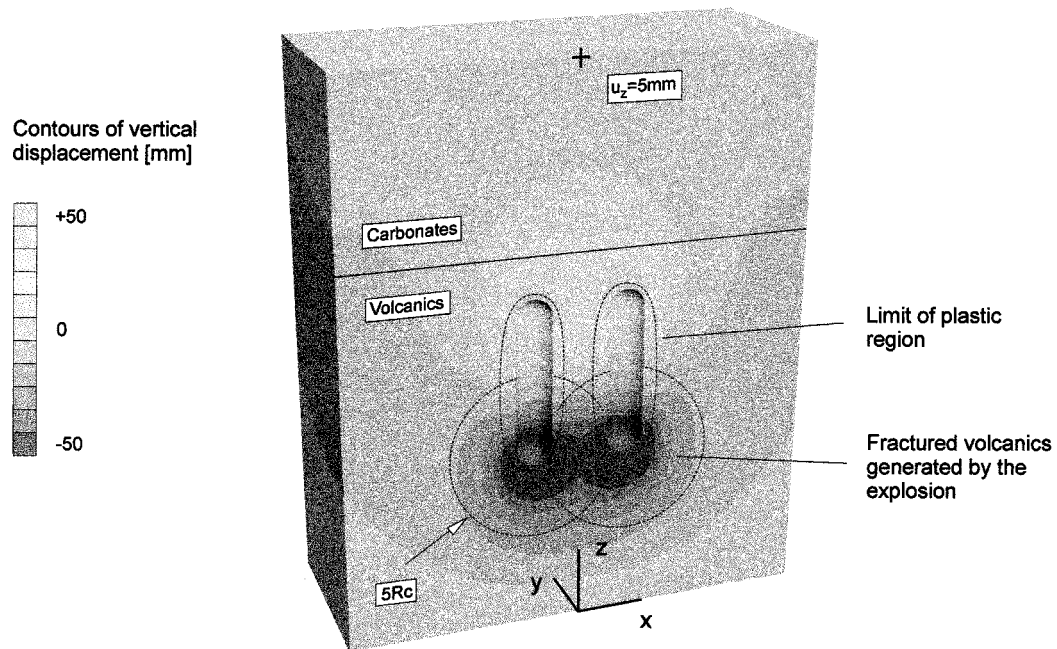
a)
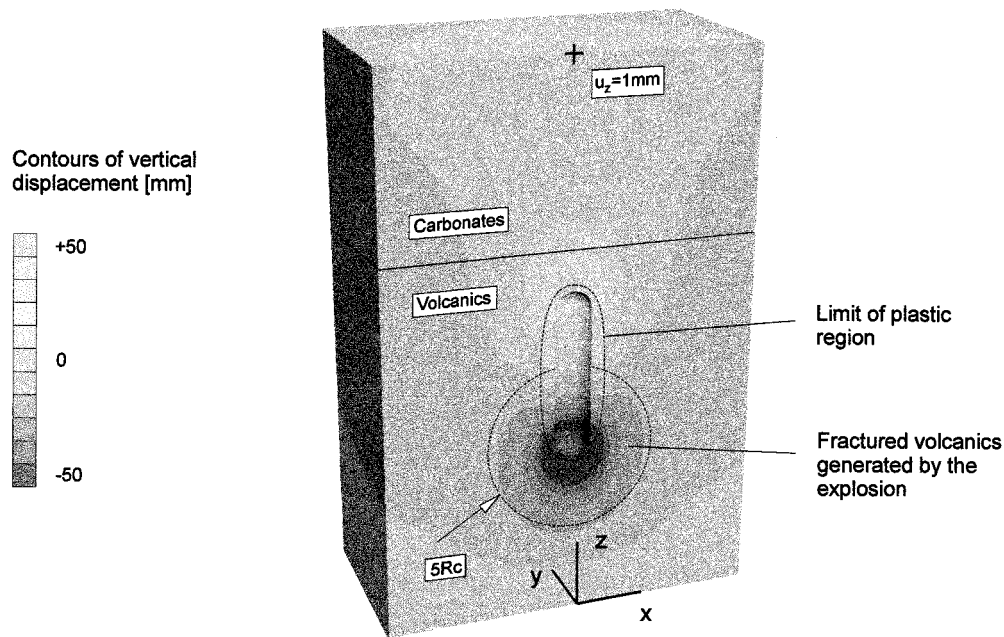
b)

Fig. 18. Damaged regions around cavities created by underground nuclear test explosions: (a) contours of vertical displacement and extent of the failed region for a single cavity; (b) results for the case of two interacting cavities (numerical analysis by FLAC^{3D} [22]).

produce deformation due to interaction between the two cavities was also of concern. An enlarged zone of rock damage developed by detonation of two explosions in close proximity to each other may result in significant increased surface deformation.

Analyses were carried out to examine the stability of (i) a single cavity and (ii) two cavities in close proximity to each other.

Although some information on the mechanical strength of rock cores was available, there was no direct knowledge available on the residual strength of the spherical zones around each crater — i.e. where

the rock had been damaged by the outgoing explosion shock wave. Accordingly, it was necessary to consider several values of residual strength in examining the ability of the underground cavities to support the overlying rock. It was not possible to inspect the damaged zone directly, so several estimated values were considered. The Hoek–Brown criterion was useful in characterizing the damaged zones and allowed a quick assessment to be made of the influence of the failed zones around each cavity for different ranges of initial and damaged rock mass strengths. Because of the complex geometries of two adjacent cavities, together with the associated collapse chimneys, it was necessary, eventually, to conduct a numerical analysis.

Fig. 17a illustrates a possible situation in which two cavities (of radii R_{c1} and R_{c2}, respectively) are separated by a distance L_c. Information reported by the IGC indicated that tests were conducted at depths up of 1000 m (and possibly 1100 m in some cases), with minimum distances between shot points of 250 m and yields sufficient to produce cavities of 50 m radii (i.e. $L_c = 250$ m and $R_{c1} = R_{c2} = 50$ m in Fig. 17a). For tests that were relatively close together, it was important to determine to what degree the fractured zone around each cavity may have overlapped and weakened the column of rock between the two rubble chimneys. In the most unfavorable situation, it was critical to know whether the cavities could stand permanently, without collapse of the overlying carbonate formations.

Before numerical models were set up, an indication of the mechanical behavior of the underground cavities was obtained from the parametric analysis presented in Section 3 of this paper.

The basalts are characterized by values of $\sigma_{ci} \simeq 75$ MPa and $m_i \simeq 17$. The vertical stress at a depth of 1000 m is $\sigma_o \simeq 28$ MPa. Since it was difficult to assess the internal support characteristics produced by the rubble material acting on the walls of the (two) chimneys when the rock mass converged onto the chimney, it was assumed, as a 'worst' case, that the cavities and chimneys remained unsupported — i.e. the rubble exerted no internal pressure ($p_i = 0$). In such a case, a range of possible values for the extension of the damaged region around the cavities can be obtained from Eq. (15) [As mentioned earlier, this part of the study considered the 'static' behavior of the cavities, well after the tests were carried out]. Considering the whole range of possible values for GSI (i.e. from 10 to 100), the Hoek–Brown parameters were first computed from Eqs. (4) and (5). Then, the maximum and minimum values of scaled far-field stresses were obtained from Eq. (10); they are $S_o = 0.55$ and 0.03, respectively. Similarly, the maximum and minimum values of scaled internal press-

ure were found to be $P_i = 2.33 \times 10^{-3}$ and 0, respectively.

Figure 17b presents an enlargement of the diagram in Fig. 8b. It is clearly seen that the maximum extension of the failed region around a spherical cavity will not be greater than approximately 1.6 times the radius of the cavity. This information, although derived under very simple assumptions, provides a useful preliminary qualitative estimate of the mechanical behavior of the openings; the number indicates that the amount of damaged material to be expected is not, for example, 10 or 20 times the radius of the (50 m or so) cavity (a magnitude that may have had major effects at the surface, located 1000 m above), but a relatively small fraction (around 60%) of the characteristic dimension, R_c, of the cavity.

The problem of mechanical interaction of the cavities and the resulting surface subsidence were studied rigorously later with the three-dimensional code FLAC^{3D}. Several different values of rock mass properties and geometries at the site were considered. The most unfavorable situation was assumed to occur for a value GSI = 10 for the fractured volcanics surrounding the shot points. As mentioned above, the walls of the cavities were assumed to be stress-free. Fig. 18a shows contours of vertical displacements for the case of a single cavity as derived from the analysis. Fig. 18b shows the contours in the case of two cavities located at the minimum separation used in the tests. In both cases, it is seen that the damaged region developing around the cavities is of limited extent, with a maximum surface depression, in the most severe case, of 5 mm (this can be compared with surface settlements of up to 2 m in some cases — due to dynamic deformation associated with the initial explosion wave). For the case of two cavities considered together, the failed region does not overlap and the contours again indicate a limited amount of subsidence (8 cm) at the surface. From the results of the complete numerical study, it is concluded that the underground cavities do not result in any significant disturbance at the ground surface.

5. Conclusions

The dimensionless form of the Hoek–Brown criterion proposed by Londe [26] provides a convenient method of incorporating this criterion into elasto-plastic analyses of rock failure.

Simplified general expressions have been obtained for the stresses, displacements and extent of the inelastic region around excavations. In the case of cylindrical and spherical cavities loaded hydrostatically, these expressions have been obtained as compact closed-form solutions.
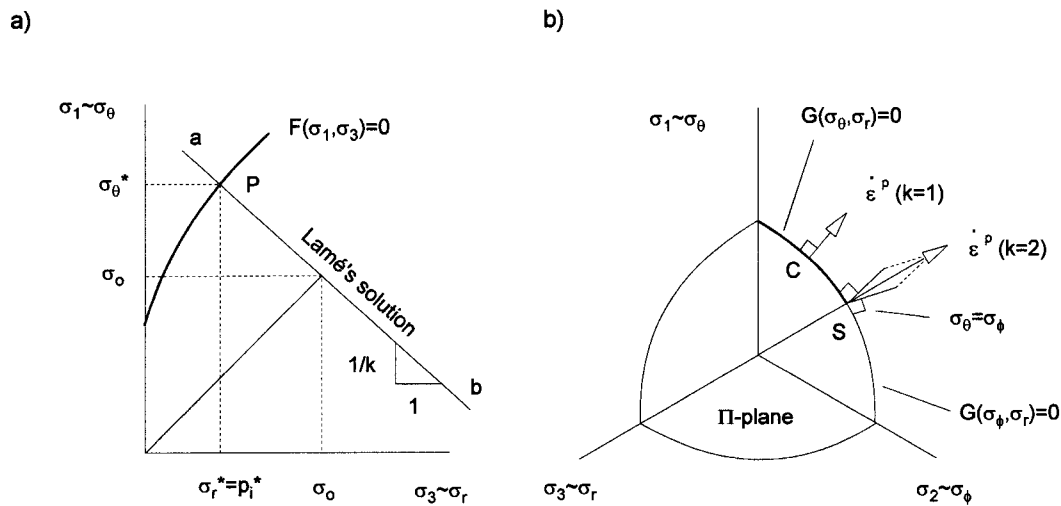
a)   b)

Fig. A1. (a) Invariance of the radial stress, σ_r^*, at the elasto-plastic interface; (b) graphical interpretation of the plastic strain vector in principal stress space. Points C and S represent the cases of cylindrical and spherical cavities respectively.

Use of the associated flow rule for Hoek–Brown materials leads to singularities in the deformation solution if the Geological Strength Index is less than 25. In this case, plastic deformation around unsupported cylindrical and spherical cavities increases without limit, independently of the value of the far-field (in situ) stress.

Dimensionless formulation of a problem provides valuable practical insight as to the relative importance of parameters that affect the result and is a valuable approach to use in numerical analysis. The implications of departures from the conditions assumed in closed-form solutions can then be assessed easily.

The procedures and results described in this paper can contribute to more effective use of the convergence–confinement method of analysis of the stability of underground openings.

Acknowledgements

The authors have appreciated and benefited considerably from discussions on the topics presented in this paper with Professor Emmanuel Detournay of the University of Minnesota.

Appendix A. Elasto-plastic solution for excavation of cylindrical and spherical openings in hydrostatic loaded medium

A.1. Problem statement

The formulation presented here is a particular case of an elasto-plastic solution discussed in Carranza-Torres [6]. The analysis is based on the incremental theory of plasticity and applies to the solution of exca-

vation of cylindrical and spherical openings in a ground initially subject to a hydrostatic stress field.

The problem under consideration is shown in Fig. 5a. A cylindrical or spherical cavity of radius b is subject to a (variable) internal pressure, p_i and hydrostatic far-field stress, σ_o; as the internal pressure is reduced below the critical value, p_i^*, a plastic region of extension $b\xi$ develops around the cavity. (The dimensionless parameter ξ defines the size of the plastic region as a proportion of the radius of the opening). Due to the symmetry of the problem, the tangential components of displacements are everywhere zero (i.e. $u_\theta = u_\phi = 0$) and the radial components of displacements, of magnitude u_r, depend only on the radial distance r.

With respect to the stresses (Fig. 5b), the tangential stresses are equal in the case of spherical openings (i.e. $\sigma_\theta = \sigma_\phi$) while, in the case of cylindrical openings, the out-of plane stress, σ_z, is an intermediate principal stress. When reduction of the internal pressure, p_i, from the initial value σ_o is considered (i.e. $p_i < \sigma_o$ in Fig. 5a), the tangential direction is a maximum principal direction and the radial direction is a minimum principal direction (i.e. for stresses $\sigma_\theta \approx \sigma_1$, $\sigma_r \approx \sigma_3$ and strains $\varepsilon_\theta \approx \varepsilon_1$, $\varepsilon_r \approx \varepsilon_3$).

Analysis of the two cases of cylindrical and spherical cavities can be treated in terms of a parameter k, where $k = 1$ denotes the case of cylindrical cavities and $k = 2$ denotes the case of spherical cavities.

A.2. Lamé's solution for the elastic region

The elastic solution for excavation of spherical or cylindrical cavities in a hydrostatically loaded medium is given by Lamé's solution (for example, Jaeger and Cook [24]).

Considering the case in which $p_i^* < p_i < \sigma_o$ (i.e. the ma-

terial is everywhere elastic), the distribution of radial and tangential stresses are, respectively,

$$\sigma_r = \sigma_o - (\sigma_o - p_i)\left(\frac{b}{r}\right)^{k+1} \tag{A.1}$$

$$\sigma_\theta = \sigma_o + \frac{1}{k}(\sigma_o - p_i)\left(\frac{b}{r}\right)^{k+1} \tag{A.2}$$

and the distribution of radial displacement is,

$$u_r = \frac{\sigma_o - p_i}{2kG}\frac{b^{k+1}}{r^k} \tag{A.3}$$

In the equation above, G is the shear modulus of the material; the other variables are as defined earlier.

For the case in which $p_i < p_i^*$, Lamé's solution applies to the elastic region that is radially beyond the elasto-plastic interface. An important feature of the solution is that the radial stress σ_r^* at the elasto-plastic interface is constant and independent of the position of the boundary. This is shown in Fig. A1a. From Lamé's solution, the stresses in the elastic region must lie on the line $\overline{ab}$. Since the yield function $\mathscr{F}(\sigma_1,\sigma_3) = 0$ is defined in terms of the stresses σ_1 and σ_3, the point of intersection between the 'elastic' line $\overline{ab}$ and the yield function defines the constant stress, σ_r^*, which must be equal to the critical internal pressure, p_i^*, for which the elastic limit is reached (i.e. $p_i^* = \sigma_r^*$).

Considering that the elasto-plastic interface has an extent of $b\xi$ and that the radial stress has the constant value σ_r^* at the interface, Lamé's solution defines the distribution of stresses and displacements within the elastic region to be

$$\sigma_r = \sigma_o - (\sigma_o - \sigma_r^*)\left(\frac{b\xi}{r}\right)^{k+1} \tag{A.4}$$

$$\sigma_\theta = \sigma_o + \frac{1}{k}(\sigma_o - \sigma_r^*)\left(\frac{b\xi}{r}\right)^{k+1} \tag{A.5}$$

Displacements (radial only)

$$u_r = \frac{\sigma_o - \sigma_r^*}{2kG}\frac{(b\xi)^{k+1}}{r^k} \tag{A.6}$$

A.3. Governing equations for the plastic region

As mentioned in Section 2, the yield condition defines the relationship between principal stresses at the moment the material starts to deform inelastically. For the problem considered here, $\sigma_\theta \approx \sigma_1$ and $\sigma_r \approx \sigma_3$ (Fig. 5b). The yield condition can thus be written as

$$\mathscr{F}(\sigma_1,\sigma_3) \simeq \mathscr{F}(\sigma_\theta,\sigma_r) = 0 \tag{A.7}$$

In order to formulate problems in plasticity, a flow rule is also needed. The flow rule can be derived from a potential that is written in terms of principal stress components, as in Eq. (A.7), i.e.

$$\mathscr{G}(\sigma_1,\sigma_3) \simeq \mathscr{G}(\sigma_\theta,\sigma_r) = 0 \tag{A.8}$$

The flow rule allows the rate of change of the principal strains to be computed.

The principal plastic-strain-rates $\dot{\varepsilon}_\theta^p$ and $\dot{\varepsilon}_r^p$ can be evaluated from the potential $\mathscr{G}(\sigma_\theta,\sigma_r)$ according to the following expressions (for example Hill [15]):

$$\dot{\varepsilon}_\theta^p = \lambda\frac{\partial\mathscr{G}}{\partial\sigma_\theta} \tag{A.9}$$

$$\dot{\varepsilon}_r^p = \lambda k\frac{\partial\mathscr{G}}{\partial\sigma_r} \tag{A.10}$$

The graphical representation of Eqs. (A.9) and (A.10) in principal stress space is shown in Fig. A1b. The plastic-strain vector components are normal to the surface defined by the potential $\mathscr{G}(\sigma_\theta,\sigma_r)$. As mentioned in Section A.1, for the case of cylindrical openings, the out-of-plane stress is assumed to be an intermediate principal stress. The vector lies on a side of the yield surface (point C in Fig. A1b). For the case of spherical cavities, the vector lies on the edge of the yield surface (point S in Fig. A1b) and the vector is defined as the resultant of the normals to each side of the junction of the two edges (for example Drescher [11]).

An important aspect of any problem in plasticity is the definition of the loading path. In the problem considered here, the loading (or, in this case, unloading) path corresponds to a monotonic decrease of the internal pressure, p_i, at the internal boundary of the opening. Since the internal pressure p_i is inversely related to the extent of the plastic region, $b\xi$, a monotonic decrease of the pressure implies a monotonic increase in extent of the elasto-plastic interface.

The incremental theory of plasticity requires the definition of a time variable to evaluate the plastic strain rates, e.g. in Eqs. (A.9) and (A.10). In the formulation presented here, the dimensionless parameter ξ will be assumed to be the time variable.

The displacement rate and strain rates can then be written as

$$\dot{u}_r = \frac{\partial u_r}{\partial\xi} \quad \dot{\varepsilon}_\theta = \frac{\partial\varepsilon_\theta}{\partial\xi} \quad \dot{\varepsilon}_r\frac{\partial\varepsilon_r}{\partial\xi} \tag{A.11}$$

Similarly, the stress rates are written as

$$\dot{\sigma}_\theta = \frac{\partial\sigma_\theta}{\partial\xi} \quad \dot{\sigma}_r = \frac{\partial\sigma_r}{\partial\xi} \tag{A.12}$$

The relationship between displacements and strains

can be derived from the conditions of compatibility of deformations. For symmetrical problems in cylindrical or spherical coordinates, these reduce to the following expressions (for example Malvern [27]):

$$\dot{\varepsilon}_\theta = \frac{\dot{u}_r}{r} \quad \dot{\varepsilon}_r = \frac{\partial \dot{u}_r}{\partial r} \tag{A.13}$$

The field quantities in the plastic region must satisfy the following governing equations and boundary conditions.

A.3.1. Equilibrium equation

Radial and tangential stresses must satisfy the differential equation of equilibrium:

$$\frac{\partial \sigma_r}{\partial r} + k\frac{\sigma_r - \sigma_\theta}{r} = 0 \tag{A.14}$$

A.3.2. Consistency equation

The consistency condition implies that the material remains in the plastic state once this state has been achieved (i.e. the total derivative of the yield function with respect to the kinematic parameter ξ must be zero). For a perfectly plastic material, this is written as

$$\frac{\partial \mathscr{F}}{\partial \sigma_r}\dot{\sigma}_r + \frac{\partial \mathscr{F}}{\partial \sigma_\theta}\dot{\sigma}_\theta = 0 \tag{A.15}$$

A.3.3. Compatibility of deformations

An elasto-plastic solution is constructed assuming that the total deformations consist of both elastic and plastic parts. Thus, the total strain rates $\dot{\varepsilon}_\theta$ and $\dot{\varepsilon}_r$ can be written in terms of elastic ($\dot{\varepsilon}_\theta^e, \dot{\varepsilon}_r^e$) and plastic ($\dot{\varepsilon}_\theta^p, \dot{\varepsilon}_r^p$) components as,

$$\dot{\varepsilon}_\theta = \dot{\varepsilon}_\theta^e + \dot{\varepsilon}_\theta^p \tag{A.16}$$

$$\dot{\varepsilon}_r = \dot{\varepsilon}_r^e + \dot{\varepsilon}_r^p \tag{A.17}$$

The relationship between the elastic components of strain rate and stress rate is given by Hooke's law (for example Sokolnikoff [34]):

$$\dot{\varepsilon}_r^e = \frac{1}{2G}\left[\frac{1-(2-k)v}{1+(k-1)v}\dot{\sigma}_r - \frac{kv}{1+(k-1)v}\dot{\sigma}_\theta\right] \tag{A.18}$$

$$\dot{\varepsilon}_\theta^e = \frac{1}{2G}\left[\frac{1-v}{1+(k-1)v}\dot{\sigma}_\theta - \frac{v}{1+(k-1)v}\dot{\sigma}_r\right] \tag{A.19}$$

Substituting the scalar λ defined by Eqs. (A.9) and (A.10) into Eqs. (A.16)–(A.19), the condition of compatibility of strain rates may be written as

$$\frac{\partial \dot{u}_r}{\partial r} - A_1\frac{\dot{u}_r}{r} = \frac{1}{2G}(A_2\dot{\sigma}_r - A_3\dot{\sigma}_\theta) \tag{A.20}$$

where

$$A_1 = k\frac{\partial \mathscr{G}/\partial \sigma_r}{\partial \mathscr{G}/\partial \sigma_\theta}$$

$$A_2 = \frac{1-(2-k)v + kv(\partial \mathscr{G}/\partial \sigma_r)/(\partial \mathscr{G}/\partial \sigma_\theta)}{1+v(k-1)}$$

$$A_3 = k\frac{(1-v)(\partial \mathscr{G}/\partial \sigma_r)/(\partial \mathscr{G}/\partial \sigma_\theta) + v}{1+v(k-1)} \tag{A.21}$$

A.3.4. Boundary conditions

In order to solve the governing Eqs. (A.14), (A.15) and (A.20) it is necessary to define the appropriate boundary conditions. Since the stresses σ_θ and σ_r and the radial displacement rate $\dot{u}_r$ are continuous across the elasto-plastic interface, the boundary conditions on the elastic side can be computed from Lamé's solution [Eqs. (A.4)–(A.6)] and then used to integrate the governing equations on the plastic side of the interface. It should be noted that the radial displacement rate, $\dot{u}_r$, is continuous only when the there is continuity of strength on each side of the interface. The case of brittle materials, for which a discontinuity in the radial velocity field exists across the interface, has been discussed in Carranza-Torres [6].

The boundary stresses are the values σ_r^* and σ_θ^* discussed earlier. As shown in Fig. A1a, the stress σ_r^* can be computed from the yield function and Lamé's solution only. If the yield function (Eq. (A.7)) is re-written as $\mathscr{F}(\sigma_\theta, \sigma_r) = \sigma_\theta - f(\sigma_r) = 0$ and substituted into the second term $(\sigma_o - \sigma_r^*)(b\xi/r)^{k+1}$ in Eqs. (A.4) and (A.5), the radial stress, σ_r^*, can be obtained from the following transcendental equation:

$$f(\sigma_r^*) = \frac{1+k}{k}\sigma_o - \frac{\sigma_r^*}{k} \tag{A.22}$$

Once σ_r^* has been determined, the stress σ_θ^* can be computed from the yield condition (Eq. (A.7)). The boundary conditions for the stresses are, therefore,

$$\sigma_r|_{r=b\xi} = \sigma_r^* \quad \sigma_\theta|_{r=b\xi} = \sigma_\theta^* \tag{A.23}$$

The boundary condition for the radial displacement is computed from Eq. (A.6) by making $r = b\xi$, i.e.

$$u_r|_{r=b\xi} = \frac{\sigma_o - \sigma_r^*}{2kG}b\xi \tag{A.24}$$

The radial displacement rate, $\dot{u}_r^*$, is evaluated from the same Eq. (A.6) by substituting it into Eq. (A.11), i.e.

$$\dot{u}_r|_{r=b\xi} = \frac{b(\sigma_o - \sigma_r^*)}{2kG}(k+1) \tag{A.25}$$

An additional boundary condition is needed in order to compute the extent $b\xi$ of the elasto-plastic interface. This condition states that the radial stress on

the wall of the cavity must be equal to the internal pressure, i.e.

$$\sigma_r|_{r=b} = p_i \tag{A.26}$$

The 'standard' approach to solving this problem would be to integrate directly the governing Eqs. (A.14), (A.15) and (A.20). This would require solving a system of partial differential equations. However, the problem can be simplified significantly by application of the properties of mechanical self-similarity, as described below.

A.4. Dimensionless form of the governing equations in the plastic region. Reduction of the time variable

The analysis that follows is based on Detournay [10].

Consider the dimensionless variable ρ that maps the physical plane (r, ξ) into a plane of coordinate ρ according to the following transformation:

$$\rho = \frac{r}{b\xi} \tag{A.27}$$

The space defined by the transformation (Eq. (A.27)) has been referred to as 'unit plane', since the plastic region is limited by a circle of unit radius (see Detournay [10]).

In the unit plane, the position of the elasto-plastic interface is fixed and given by $\rho = 1$, while the wall of the cavity, defined by $\rho = 1/\xi$, moves inward as the plastic zone grows around the cavity.

The problem introduced earlier in Section A.1 is said to be (mechanically) self-similar when the transformation (Eq. (A.27)) is considered (for example Barenblatt [2]). For this case, the governing Eqs. (A.14), (A.15) and (A.20) contain the variable ρ as a similarity variable (i.e. ξ disappears from the governing equations when the transformation (Eq. (A.27)) is applied).

In order to work with dimensionless field quantities, the stress magnitude, $\sigma_o - \sigma_r^*$ in Fig. A1a, is used to normalize the stresses:

$$\tilde{\sigma}_\theta = \frac{\sigma_\theta}{\sigma_o - \sigma_r^*} \quad \tilde{\sigma}_r = \frac{\sigma_r}{\sigma_o - \sigma_r^*} \tag{A.28}$$

Strains are normalized accordingly, considering the extra term $2kG$:

$$\tilde{\varepsilon}_\theta = \frac{2kG}{\sigma_o - \sigma_r^*}\varepsilon_\theta \quad \tilde{\varepsilon}_r = \frac{2kG}{\sigma_o - \sigma_r^*}\varepsilon_r \tag{A.29}$$

Displacements are normalized in terms of the radius b:

$$\tilde{u}_r = \frac{2kG}{b(\sigma_o - \sigma_r^*)}u_r \tag{A.30}$$

Given transformation (Eq. (A.27)), the partial derivatives of the field functions with respect to the variables r and ξ are evaluated with the operators:

$$\frac{\partial(\ )}{\partial r} = \frac{1}{b\xi}\frac{\mathrm{d}(\ )}{\mathrm{d}\rho} \tag{A.31}$$

$$\frac{\partial(\ )}{\partial \xi} = -\frac{\rho}{\xi}\frac{\mathrm{d}(\ )}{\mathrm{d}\rho} \tag{A.32}$$

In the unit plane, the *equilibrium* condition Eq. (A.14) is then expressed as

$$\frac{\mathrm{d}\tilde{\sigma}_r}{\mathrm{d}\rho} + k\frac{\tilde{\sigma}_r - \tilde{\sigma}_\theta}{\rho} = 0 \tag{A.33}$$

Similarly, the *consistency* condition Eq. (A.15) is written as

$$\frac{\partial\mathcal{F}}{\partial\sigma_r}\frac{\mathrm{d}\tilde{\sigma}_r}{\mathrm{d}\rho} + \frac{\partial\mathcal{F}}{\partial\sigma_\theta}\frac{\mathrm{d}\tilde{\sigma}_\theta}{\mathrm{d}\rho} = 0 \tag{A.34}$$

and the *compatibility* condition Eq. (A.20), as

$$\frac{\mathrm{d}\tilde{\tilde{u}}_r}{\mathrm{d}\rho} - A_1\frac{\tilde{\tilde{u}}_r}{\rho} = -\rho k\left(A_2\frac{\mathrm{d}\tilde{\sigma}_r}{\mathrm{d}\rho} - A_3\frac{\mathrm{d}\tilde{\sigma}_\theta}{\mathrm{d}\rho}\right) \tag{A.35}$$

with A_1, A_2 and A_3 defined by Eq. (A.21).

Using the definition (Eq. (A.28)), the boundary condition for the stresses at the elasto-plastic boundary takes the form

$$\tilde{\sigma}_r(1) = \tilde{\sigma}_o - 1 \tag{A.36}$$

while the boundary condition for the radial velocity is

$$\tilde{\tilde{u}}_r(1) = k + 1 \tag{A.37}$$

Note that, since the transformed governing Equations (A.33), (A.34) and (A.35) depend only on the dimensionless variable ρ, the radial displacement, $u_r(r, \xi)$, in the physical plane must be related to the velocity by the expression

$$u_r(r, \xi) = \xi\frac{b(\sigma_o - \sigma_r^*)}{2kG}\tilde{u}_r(\rho) \tag{A.38}$$

Using the operator defined in Eq. (A.32), the relationship between radial displacement rate and radial displacements in the unit plane is given by

$$\tilde{\tilde{u}}_r = \tilde{u}_r - \rho\frac{d\tilde{u}_r}{d\rho} \tag{A.39}$$

The governing Eqs. (A.14), (A.15) and (A.20), originally expressed in partial derivatives, have now been reduced to ordinary differential equations — in particular, Eq. (A.39), relating the velocity and the displacement fields, allows these equations to be written in

terms of the functions $\tilde{\sigma}_r$, $\tilde{\sigma}_\theta$ and $\tilde{u}_r$ only (i.e. a straight-forward integration of the velocity field, $\tilde{\dot{u}}_r$).

In summary, the *equilibrium*, *consistency* and *compatibility* equations reduce to

$$\frac{\mathrm{d}\tilde{\sigma}_r}{\mathrm{d}\rho} = -k\frac{\tilde{\sigma}_r - \tilde{\sigma}_\theta}{\rho} \qquad (A.40)$$

$$\frac{\mathrm{d}\tilde{\sigma}_\theta}{\mathrm{d}\rho} = -\frac{\partial\mathcal{F}/\partial\sigma_r}{\partial\mathcal{F}/\partial\sigma_\theta}\frac{\mathrm{d}\tilde{\sigma}_r}{\mathrm{d}\rho} \qquad (A.41)$$

$$\frac{\mathrm{d}^2\tilde{u}_r}{\mathrm{d}\rho^2} = A_2 k\frac{\mathrm{d}\tilde{\sigma}_r}{\mathrm{d}\rho} - A_3 k\frac{\mathrm{d}\tilde{\sigma}_\theta}{\mathrm{d}\rho} + \frac{A_1}{\rho}\frac{\mathrm{d}\tilde{u}_r}{\mathrm{d}\rho} - A_1\frac{\tilde{u}_r}{\rho^2} \qquad (A.42)$$

The boundary condition for the radial stress is the same as in Eq. (A.36), while the boundary conditions for the displacement field are derived from Eqs. (A.24), (A.25) and (A.39):

$$\tilde{u}_r(1) = 1 \qquad (A.43)$$

$$\tilde{u}_r'(1) = -k \qquad (A.44)$$

In the equations above, $\tilde{u}_r'(1)$ represents the first derivative of the displacement with respect to the similarity variable, ρ (evaluated at the elasto-plastic interface).

Solution of the system of Eqs. (A.40)–(A.42), together with the boundary conditions Eqs. (A.36), (A.43) and (A.44), gives the distribution of the field quantities $\tilde{\sigma}_r$, $\tilde{\sigma}_\theta$ and $\tilde{u}_r$ in the unit plane.

The field quantities in the physical plane are computed by application of the inverse of the transformation (Eq. (A.27)). The normalized radius of the elasto-plastic interface, ξ, is first computed using the condition (Eq. (A.26)); i.e. $\tilde{\sigma}_r(1/\xi) = \tilde{p}_i$.

A.5. Closed-form solution for the plastic region using the normalized form of the Hoek–Brown failure criterion

According to Eqs. (2) and (A.7), the Hoek–Brown yield condition can be written as

$$\mathcal{F}(\sigma_\theta,\sigma_r) = \sigma_\theta - \sigma_r - \sigma_{ci}\left(m_b\frac{\sigma_r}{\sigma_{ci}} + s\right)^a = 0 \qquad (A.45)$$

The parameters σ_{ci}, m_b, a and s were discussed and defined in Section 2, where it was shown that a general dimensionless form of the Hoek–Brown failure criterion could be obtained by appropriate scaling of the principal stress components.

In the elasto-plastic analysis presented here, the transformations shown in Eq. (8) of the main text are applied to the stress field and to the boundary conditions. The transformed radial and tangential stresses

are, then,

$$S_\theta = \frac{\sigma_\theta}{m_b\sigma_{ci}} + \frac{s}{m_b^2} \qquad S_r = \frac{\sigma_r}{m_b\sigma_{ci}} + \frac{s}{m_b^2} \qquad (A.46)$$

and the transformed internal pressure and far-field stress are

$$P_i = \frac{p_i}{m_b\sigma_{ci}} + \frac{s}{m_b^2} \qquad S_o = \frac{\sigma_o}{m_b\sigma_{ci}} + \frac{s}{m_b^2} \qquad (A.47)$$

Using the expressions in Eq. (A.46), the transformed stress rates are related to the original stress rates as follows:

$$\dot{S}_\theta = \frac{\dot{\sigma}_\theta}{m_b\sigma_{ci}} \qquad \dot{S}_r = \frac{\dot{\sigma}_r}{m_b\sigma_{ci}} \qquad (A.48)$$

Also, to be consistent with the definition of elastic strains rates given by Eqs. (A.18) and (A.19), the shear modulus will be scaled according to the expression

$$\gamma = \frac{G}{m_b\sigma_{ci}} \qquad (A.49)$$

When the stress components defined by Eq. (A.46) are considered, the yield condition (Eq. (A.45)) may be written as

$$\mathcal{F}(S_\theta,S_r) = S_\theta - S_r - \sqrt{S_r} = 0 \qquad (A.50)$$

In order to use the same boundary conditions given in Eqs. (A.36), (A.43) and (A.44) in the unit plane of coordinate ρ, stresses will be normalized as in Eq. (A.28), i.e.

$$\tilde{S}_\theta = \frac{S_\theta}{S_o - S_r^*} \qquad \tilde{S}_r = \frac{S_r}{S_o - S_r^*} \qquad (A.51)$$

and displacements as in Eq. (A.30), i.e.

$$\tilde{U}_r = \frac{2k\gamma}{b(S_o - S_r^*)}u_r \qquad (A.52)$$

Considering the definition Eq. (A.49), the normalized displacement $\tilde{U}_r$, defined above, is equal to the displacement $\tilde{u}_r$, defined in Eq. (A.30), i.e. $\tilde{U}_r = \tilde{u}_r$.

With the above transformations, the system of governing Eqs. (A.40)–(A.42) becomes,

$$\frac{\mathrm{d}\tilde{S}_r}{\mathrm{d}\rho} = -k\frac{\tilde{S}_r - \tilde{S}_\theta}{\rho} \qquad (A.53)$$

$$\frac{\mathrm{d}\tilde{S}_\theta}{\mathrm{d}\rho} = -\frac{\partial\mathcal{F}/\partial S_r}{\partial\mathcal{F}/\partial S_\theta}\frac{\mathrm{d}\tilde{S}_r}{\mathrm{d}\rho} \qquad (A.54)$$

$$\frac{\mathrm{d}^2\tilde{u}_r}{\mathrm{d}\rho^2} = A_2 k\frac{\mathrm{d}\tilde{S}_r}{\mathrm{d}\rho} - A_3 k\frac{\mathrm{d}\tilde{S}_\theta}{\mathrm{d}\rho} + \frac{A_1}{\rho}\frac{\mathrm{d}\tilde{u}_r}{\mathrm{d}\rho} - A_1\frac{\tilde{u}_r}{\rho^2} \qquad (A.55)$$

where the coefficients A_1, A_2 and A_3 depend on the flow rule chosen (Eq. (A.21)).

For the case of perfectly plastic behavior considered here, the problem defined by the governing Eqs. (A.53)–(A.55) is statically determined (i.e. the stresses can be solved independently of the displacements).

The solution for the stress field is as follows.

The magnitude S_r^* used to scale the stress components in Eq. (A.51) can be computed from Eq. (A.22) and written as

$$S_r^* + \sqrt{S_r^*} = \frac{1+k}{k} S_o - \frac{S_r^*}{k} \tag{A.56}$$

Solution of the transcendental equation above gives

$$S_r^* = \left[\frac{k - \sqrt{k^2 + 4(k+1)^2 S_o}}{2(k+1)} \right]^2 \tag{A.57}$$

As mentioned earlier, in Section A.2, the stress S_r^* is also equal to the scaled critical internal pressure that triggers the development of a plastic region around the opening.

The first differential equation to be solved is Eq. (A.54). For perfectly plastic problems, the solution is given simply by the scaled tangential stress derived from the yield function (Eq. (A.45)), i.e.

$$\tilde{S}_\theta = \tilde{S}_r + \sqrt{\frac{\tilde{S}_r}{S_o - S_r^*}} \tag{A.58}$$

The distribution of radial stresses can now be obtained by solving the differential Equation (A.53) using relationship Eq. (A.58) and the boundary condition Eq. (A.36), scaled according to the transformation Eq. (A.47), i.e. $\tilde{S}_r(1) = \tilde{S}_o - 1$. The solution is found to be

$$\tilde{S}_r(\rho) = \left[\sqrt{\tilde{S}_r^*} + \frac{k}{2\sqrt{S_o - S_r^*}} \ln(\rho) \right]^2 \tag{A.59}$$

The extent of the plastic region is found by considering the boundary condition Eq. (A.26) with the transformed internal pressure in the solution Eq. (A.59), i.e. $\tilde{S}_r(1/\xi) = \tilde{P}_i$, where $\tilde{P}_i$ is the internal pressure, Eq. (A.47), scaled according to Eq. (A.51). Application of solution Eq. (A.59) with the above-mentioned boundary condition leads to the following expression:

$$\xi = \exp\left[\frac{2}{k} \left(\sqrt{S_r^*} - \sqrt{P_i} \right) \right] \tag{A.60}$$

With the stress field defined by Eqs. (A.58) and (A.59), displacements can be obtained by solving the differential Eq. (A.55). In order to evaluate the coeffi-

cients A_1, A_2 and A_3, it is necessary to define a flow rule.

Most of the existing analyses that use the Hoek–Brown failure criterion assume a linear or 'non-associated flow' rule in which the dilation angle is constant. This arises naturally when solving for Mohr–Coulomb plastic models (for example Brady and Brown [4]). An alternative approach is to assume a normal or 'associated flow' rule. In this case, the potential has the same form as the yield function and no extra parameters need to be introduced (Pan and Hudson [30]). The latter choice may also be justified on the basis of normality of the plastic components of deformation observed in triaxial tests on sand and clays (for example Wood [36]).

In the present study, both flow rules will be considered; the case of a nonassociated flow rule will be discussed first and the associated flow rule will be considered later.

The linear non-associated flow rule can be derived from the following potential:

$$\mathcal{G}(S_\theta, S_r) = S_\theta - K_p^* S_r = 0 \tag{A.61}$$

In the equation above, the parameter K_p^* depends on the dilation angle ψ according to the relationship

$$K_p^* = \frac{1 + \sin \psi}{1 - \sin \psi} \tag{A.62}$$

The solution for displacements can then be derived from the differential Eq. (A.55), which, when considered in conjunction with Eqs. (A.58) and (A.59), takes the form

$$\rho^2 \frac{d^2 \tilde{u}_r}{d\rho^2} - A_1 \rho \frac{d\tilde{u}_r}{d\rho} + A_1 \tilde{u}_r - \mathcal{B}(\rho) = 0 \tag{A.63}$$

where

$$A_1 = -kK_p^* \quad A_2 = \frac{1 - (2-k)v - kvK_p^*}{1 + v(k-1)}$$

$$A_3 = k\frac{v - (1-v)K_p^*}{1 + v(k-1)} \tag{A.64}$$

and,

$$\mathcal{B}(\rho) = \frac{\rho k^2}{S_o - S_r^*} \left[\sqrt{S_r^*} + \frac{k}{2} \ln(\rho) \right]$$
$$\times \left[A_2 - A_3 - \frac{A_3}{2\sqrt{S_r^*} + k \ln(\rho)} \right] \tag{A.65}$$

Equation (A.63) is a linear non-homogeneous, second-order differential equation of the Cauchy type. Solution of this equation, together with the boundary conditions Eqs. (A.43) and (A.44), leads to

$$\tilde{u}_r(\rho) = \frac{A_1 + k}{A_1 - 1}\rho$$

$$+ \left[\frac{k^2\mathscr{D}}{2(S_o - S_r^*)(1 - A_1)^3} - \frac{k+1}{A_1 - 1} \right]\rho^{A_1}$$

$$+ \frac{k^3\mathscr{C}}{4(S_o - S_r^*)(1 - A_1)}\rho \ln(\rho)^2$$

$$+ \frac{k^2\mathscr{D}}{2(S_o - S_r^*)(1 - A_1)^3}\rho[(1 - A_1)\ln(\rho) - 1] \quad \text{(A.66)}$$

where

$$\mathscr{C} = A_2 - A_3$$

$$\mathscr{D} = A_2\left[2\sqrt{S_r^*}(1 - A_1) - k\right]$$
$$\quad - A_3\left[2\sqrt{S_r^*}(1 - A_1) + (1 - A_1) - k\right] \quad \text{(A.67)}$$

The displacements in the physical plane of coordinates r and ξ can then be obtained by first taking the inverse of the transformation Eq. (A.27). The values obtained from solution Eq. (A.66) are then multiplied by ξ according to Eq. (A.38).

The problem can also be formulated to account for an associated flow rule. In this case, the potential is the same as the yield function Eq. (A.50), i.e.

$$\mathscr{G}(S_\theta, S_r) = S_\theta - S_r - \sqrt{S_r} = 0 \quad \text{(A.68)}$$

To solve for displacements, the same differential Eq. (A.63) is considered, but with the coefficients

$$A_1 = -k\left(1 + \frac{1}{2\sqrt{S_r}}\right)$$

$$A_2 = \frac{1 - (2 - k)v - kv\left(1 + \dfrac{1}{2\sqrt{S_r}}\right)}{1 + v(k - 1)}$$

$$A_3 = k\frac{v - (1 - v)\left(1 + \dfrac{1}{2\sqrt{S_r}}\right)}{1 + v(k - 1)} \quad \text{(A.69)}$$

Since the relationship between the coefficient A_1 and the variable ρ is logarithmic [Eq. (A.59)], the governing Eq. (A.63) now becomes a nonlinear differential equation. A solution to this equation can be obtained by application of standard numerical integration algorithms. In this study, the Runge–Kutta method was used (for example, Press et al. [37]); the results, evaluated at $\rho = 1/\xi$ (i.e. at the wall of the cavities), are summarized in the diagrams of Fig. 11.

It should be noted that, under certain conditions, the use of an associated flow may lead to a singular behavior for the displacements. This is illustrated by considering how the rate of plastic volumetric strain is related to the stress field. In the symmetrical problem considered here, the volumetric strain rate $\dot{\varepsilon}^p$ is defined as

$$\dot{\varepsilon}^{\,p} = \dot{\varepsilon}_r^p + \dot{\varepsilon}_\theta^p \quad \text{(A.70)}$$

Considering the relationships Eqs. (A.9) and (A.10), together with the potential (Eq. (A.68)), the volumetric strain is found to be related to the minimum principal stress according to the relationship

$$\dot{\varepsilon}^p = \left(1 - k - \frac{k}{2\sqrt{S_r}}\right)\dot{\varepsilon}_\theta^p \quad \text{(A.71)}$$

It is evident from Eq. (A.71) that, in the limit, as S_r tends to zero, the plastic volumetric strain rate becomes infinite and the material 'flows' in a manner similar to a critical state in soil mechanics. The problem has also been encountered in the implementation of an associated flow rule for the Hoek–Brown constitutive model in the finite difference code FLAC^{3D} [9]. In the problem of excavating cylindrical or spherical openings, the conditions that lead to a zero value for S_r are zero confining pressure and a zero value of the parameter s (Eq. (A.46)). This condition can be expected at the wall of unsupported cavities in rock masses of very low quality (according to Eq. (5), when GSI < 25). This is essentially the situation in which the material is cohesionless. At zero radial stress (i.e. an unsupported cavity), the material cannot support a tangential stress at the boundary. Under such conditions, it is simply not possible to maintain an unsupported cavity.

References

[1] Anagnostou G, Kovari K. Significant parameters in elastoplastic analysis of underground openings. ASCE J Geotech Eng Div 1993;119(3):401–19.

[2] Barenblatt GI. Dimensional analysis. Gordon and Breach Science Publishers, 1987.

[3] Bieniawski ZT. Rock mass classification in rock engineering. In: Bieniawski ZT, editor. Proc. of the Symp. in Exploration for Rock Engineering, Cape Town. Balkema, 1976. p. 97–106.

[4] Brady BGH, Brown ET. Rock mechanics for underground mining, 2nd ed. Chapman and Hall, 1993.

[5] Brown ET, Bray JW, Landayi B, Hoek E. Ground response curves for rock tunnels. ASCE J Geotech Eng Div 1983;109(1):15–39.

[6] Carranza-Torres C. Self-similarity analysis of the elasto-plastic response of underground openings in rock and effects of practical variables. Ph.D. thesis, University of Minnesota, 1998.

[7] Chern JC, Shiao FY, Yu CW. An empirical safety criterion for tunnel construction. In: Proc. Regional Symposium on Sedimentary Rock Engineering. Nov 20–22 1998, Taipei, Taiwan. Balkema, 1998. p. 222–7.

[8] Collins IF, Stimpson JR. Similarity solutions for drained and undrained cavity expansions in soils. Géotechnique 1994;44(1):21–34.

[9] Cundall P, Detournay C, Hart R, Russell D. Personal communication. Software Development Group. Itasca. Minneapolis, 1998.

[10] Detournay E. Elastoplastic model of a deep tunnel for a rock with variable dilatancy. Rock Mech Rock Eng 1986;19:99–108.

[11] Drescher A. Analytical methods in bin–load analysis. Amsterdam: Elsevier, 1991.

[12] Duncan Fama ME. Numerical modelling of yield zones in weak rock. In: Hudson JA, editor. Comprehensive rock engineering, 2. Oxford: Pergamon, 1993. p. 49–75.

[13] Fairhurst C, Brown ET, de Marsily G, Detournay E, Nikolaevskiy V, Pearson JRA, Townley L. Underground Nuclear Testing in French Polynesia: Stability and Hydrology Issues. Report of the International Geomechanical Commission to the French Government. Vol I and II. November 1998.

[14] Goodman RE. Introduction to rock mechanics. New York: Wiley and Sons, 1980.

[15] Hill R. The mathematical theory of plasticity. Oxford Science Publications, 1950.

[16] Hoek E, Brown ET. Underground excavations in rock. London: The Institute of Mining and Metallurgy, 1980.

[17] Hoek E, Brown ET. Practical estimates of rock mass strength. Int J Rock Mech Min Sci Geomech Abstr 1997;34(8):1165–86.

[18] Hoek E, Wood D, Shah S. A modified Hoek–Brown criterion for jointed rock masses. In: Hudson JA, editor. Proc. Rock Characterization, Symp. Int. Soc. Rock Mech.: Eurock '92. London: British Geotechnical Society, 1992. p. 209–14.

[19] Hoek E, Kaiser PK, Bawden WF. Support of underground excavations in hard rock. Rotterdam: Balkema, 1995.

[20] Hoek E. Reliability of Hoek–Brown estimates of rock mass properties and their impact on design. Int J Rock Mech Min Sci and Geomech Abstr 1998;35(1):63–8.

[21] Hoek, E. (1999). Personal Communication.

[22] Itasca Consulting Group. FLAC3D, Fast Lagrangian Analysis of Continua in 3 Dimensions. Version 2.0. Minneapolis, 1997.

[23] Itasca Consulting Group. 3DEC, 3 Dimensional Distinct Element Code. Version 2.0. Minneapolis, 1998.

[24] Jaeger JC, Cook NGW. Fundamentals of rock mechanics. London: John Wiley and Sons, 1976.

[25] Karzulovic A, Diaz A. Evaluación de las propiedades geomecánicas de la Brecha Braden en mina El Teniente. In: IV Congreso Sudamericano de Mecánica de Rocas, Santiago. 1994 vol. 1, p. 39-47.

[26] Londe P. Discussion on the determination of the shear stress failure in rock masses. ASCE J Geotech Eng Div 1988;114(3):374–6.

[27] Malvern LE. Introduction to the mechanics of a continuous medium. New Jersey: Prentice-Hall, Inc, 1969.

[28] Moretto O, Sarra-Pistone RE, del Rio JC. A case history in Argentina. Rock mechanics for underground works in the pumping storage development of Rio Grande No 1. In: Hudson JA, editor. Comprehensive rock engineering, 5. Oxford: Pergamon, 1993. p. 159–92.

[29] Mühlhaus HB. Lower bound solutions for circular tunnels in two and three dimensions. Rock Mech Rock Eng 1985;18:37–52.

[30] Pan XD, Hudson JA. A simplified three dimensional Hoek–Brown yield condition. In: Romana M, editor. Rock mechanics and power plants. Proc. ISRM Symp. Rotterdam: Balkema, 1988. p. 95–103.

[31] Panet M. Calcul des tunnels par la méthode de Convergence–Confinement. Press de l'école Nationale des Ponts et Chaussées, 1995.

[32] Papanastasiou P, Durban D. Elastoplastic analysis of cylindrical cavity problems in geomaterials. Int J Numer Anal Methods Geomech 1997;21:133–49.

[33] Serafim JL, Pereira JP. Consideration of the geomechanical classification of Bieniawski. In: Proc. Int. Symp. on Engineering Geology and Underground Construction, Lisbon. 1983, vol. 1(II), p. 33-44.

[34] Sokolnikoff I. Mathematical theory of elasticity. New York: Mc. Graw Hill, 1956.

[35] Wang Y. Ground response of a circular tunnel in poorly consolidated rock. ASCE J Geotech Eng 1996;122(9):703–8.

[36] Wood DM. Soil behaviour and critical state in soil mechanics, 1st ed. Cambridge University Press, 1990.

[37] Press WH, Flannery BP, Teukolsky SA, Vetterling WT. Numerical recipes in C: the art of scientific computing. Cambridge University Press, 1994.